



저작자표시-비영리-변경금지 2.0 대한민국

이용자는 아래의 조건을 따르는 경우에 한하여 자유롭게

- 이 저작물을 복제, 배포, 전송, 전시, 공연 및 방송할 수 있습니다.

다음과 같은 조건을 따라야 합니다:



저작자표시. 귀하는 원저작자를 표시하여야 합니다.



비영리. 귀하는 이 저작물을 영리 목적으로 이용할 수 없습니다.



변경금지. 귀하는 이 저작물을 개작, 변형 또는 가공할 수 없습니다.

- 귀하는, 이 저작물의 재이용이나 배포의 경우, 이 저작물에 적용된 이용허락조건을 명확하게 나타내어야 합니다.
- 저작권자로부터 별도의 허가를 받으면 이러한 조건들은 적용되지 않습니다.

저작권법에 따른 이용자의 권리는 위의 내용에 의하여 영향을 받지 않습니다.

이것은 [이용허락규약\(Legal Code\)](#)을 이해하기 쉽게 요약한 것입니다.

[Disclaimer](#)

공학박사학위논문

**나노 / 마이크로 스케일의 엔지니어링
구조를 통한 고 유연성 / 신축성 은 나
노 와이어 기반 투명 전극 제작**

**Fabrication of Highly Flexible and Stretchable Silver
Nanowires Based Transparent Conductor Through
Engineering Structure at Nano/Micro-scales**

2021년 2월

서울대학교 대학원

기계항공공학부

원 필 립

**Fabrication of Highly Flexible / Stretchable Silver
Nanowires Based Transparent Conductor Through
Engineering Structure at Nano / Micro-scales**

지도교수 고 승 환

이 논문을 공학박사 학위논문으로 제출함

2021년 2월

서울대학교 대학원

기계항공공학부

원 필 립

원필립의 공학박사 학위논문을 인준함

2020년 10월

위 원 장 : 신 용 대

부위원장 : 고 승 환

위 원 : 이 윤 석

위 원 : 홍 석 준

위 원 : 이 하 범

Abstract

As the demand for next generation electronic devices rapidly changes its form from functional and high performances devices to flexible and compliant devices, stretchable electronics have been developed to be lightweight, flexible and even stretchable. Flexible/stretchable electronics recently have shown great potential that will greatly expand the domain of electronics to mechanically deformable displays, wearable, bio-integrated devices and sensors for human-machine interface (HMI) that bridges between human and machine. Compared to traditional rigid silicon based electronics, stretchable electronics devices can maintain their functionality under mechanical deformation such as twisting, bending, compression and stretching. The core technology that enables this electronic system involve development of deformable electrodes, which are an essential component for circuits, devices and sensors. Future electronics will be fully soft and interactive depending on how we fabricate and design the electrodes. Therefore, the efforts in flexible and stretchable electrodes have been largely focused on improving two essential performances, electrical property and mechanical property. My dissertation focuses on developing highly flexible/stretchable silver nanowires (AgNWs) based conductive electrode that exhibits excellent electrical and mechanical property, even while demonstrating highly transparent optical property, to expand the scope of stretchable electronics.

In this dissertation, synthesis of AgNWs is studied to provide NWs with different dimensions for structural advantages both at nano-micro-scale in order to fabricate high quality transparent electrodes. Then, a solution-based fabrication approach that both dramatically reduces contact resistance between NW to NW and enhances NWs adhesion to the substrate by welding / embedding effect that simultaneous occur. This fabrication approach is ii

achieved by coating a swellable polymer layer on a substrate. This process has enabled a scalable fabrication of high performance NWs percolation network conductor through welding and embedding at a room temperature. Lastly, a kirigami design approach to engineer AgNWs based transparent flexible conductor into elastic stretchable conductors is demonstrated. These engineered transparent electrodes patterned by different kirigami design have shown that they can be applied to a series of wearable applications, including stretchable heater, electrophysiology (EP) sensing electrodes and human-machine interface electronic-skin (E-skin).

Keyword : (within 6 words) Flexible/stretchable electrode, silver nanowires (AgNWs), scalable fabrication, kirigami design, electronic skin (E-Skin).

Student Number : 2015-20738

Table of Contents

Abstract	ii,iv
List of Figures	1
Chapter 1. Introduction.....	7
1.1 Background	
1.2 Purpose of research	
Chapter 2. Fabrication of Highly flexible Ag nanowire based transparent electrode	11
2.1 Demand for Ag nanowire based transparent flexible electrode as an alternative to ITO	
2.2 Dual-scale silver nanowires based transparent electrode	
2.2.1 Integration of silver nanowires at different length scales	
2.2.2 Dual-scale Ag nanowire based transparent electrode as organic light emitting diode (OLED) application	
2.2.3 Experimental section for dual-scale NW transparent electrode	
2.3. Contact resistance of nanowire to nanowire	
2.3.1 Room temperature fabrication of Ag nanowire based high performance transparent electrode	
2.3.2 Effect of PU layer on the performance of Ag nanowire based flexible transparent electrode	
2.3.3 Coating of NW based transparent conductor on diverse substrates	
2.3.4 Experimental section for room-temperature post-treatment for high performance AgNWs transparent electrode	
2.4 Fabrication of organic light emitting diode (OLED) using NWs based transparent electrode	
2.5 Conclusion	
Chapter 3. Design engineering for Ag nanowire based transparent stretchable electrode	41
3.1 Background	
3.2 Kirigami structure for engineering applications	
3.2.1 Kirigami engineering of transparent electrode	
3.2.2 Force analysis of uni-axial kirigami structure	
3.2.2 Mechanical property of transparent kirigami electrode	
3.2.3 Applications of stretchable transparent kirigami electrode	
3.2.3.1 Stretchable transparent kirigami heater	
3.2.3.2 Stretchable transparent kirigami electrophysiology (EP) sensor	
3.2.3.3 Human-machine interface using TKE	
3.2.3.4 Experimental section for stretchable transparent kirigami electrode	
3.3 Conclusion	
Chapter 4. Summary and Future Work.....	74
Bibliography	76
Abstract in Korean	84

List of Figures

Figure 1 Growing need for alternative transparent electrodes as the form of electronics starting to change from rigid to flexible. Candidates for alternative to ITO are carbon nanotubes, silver nanowires (AgNWs) and graphene. Market speculation of transparent conductors by the products. (Right)

Figure 2 Electronics from the past to the future.

Figure 3 Research focus for the development multifunctional high performance silver nanowire based flexible / stretchable transparent conductor.

Figure 4 Concept of a dual-scale Ag nanowires based transparent electrode.

Figure 5 Optical properties of silver nanowires at different length and diameters. a) Transmittance vs sheet resistance, b) Haze vs. sheet resistance.

Figure 6 SEM pictures of synthesized a) short/thin AgNWs (10 μm / 40 nm) and b) long/thick AgNWs (100 μm / 100 nm).

Figure 7 SEM and AFM images of fabricated silver nanowire based transparent conductor (a) dual-scale NWs (b) long/thick NWs and (c) short/thin NWs.

Figure 8 Transformed and counted SEM images based on different coating ratio by segmentation in Image Pro..

Figure 9 AFM topography of AgNWs network before embedding a) long/thick AgNWs b) short/thin AgNWs c) dual-scale AgNWs and corresponding roughness before/after embedding.

Figure 10 a) Spectral transmittance of dual-scale AgNWs (blue), long/thick AgNWs (red) and short/thin AgNWs (green). b) Digital image of a transparent conductor using dual-scale AgNWs.

Figure 11 Stability of the embedded dual-scale AgNWs based transparent electrode. a) Adhesion test by tape test, b) mechanical stability test by cyclic bending and c) chemical stability test in an air plasma environment.

Figure 12 a) UV resistant test of embedded NWs versus NWs on a bare glass substrate under 40 W plasma treatment. b) UV failure test of embedded NWs under 40 and 1000 W plasma power treatment condition.

Figure 13 Illustration of dual-scale AgNW network transparent conductor fabrication process and its application for flexible OLED demonstration.

Figure 14 Schematic illustration of the OLED layers along with a digital image and energy diagram of OLED structure.

Figure 15 OLED characterization in (a) current density and luminance, (b) power efficiency, (c) external quantum efficiency (hollow symbols) and current efficiency (solid symbols) and (d) normalized electroluminescence spectra (at the current density of 25mA/cm²) from OLEDs using three different types of AgNW network transparent conductors (short AgNWs, long AgNWs, dual-scale AgNWs).

Figure 16 a) Current efficiency and b) power efficiency comparisons (black bars: previous OLED with a single sized AgNW transparent electrode, red bars: current work with a dual-scale AgNW transparent electrode).

Figure 17 Proposed welding approaches for NW contact resistant improvements.

Figure 18 Steps that undergoes for a swellable polymer layer assistive welding / embedding at room temperature.

Figure 19 Effect of rolling before/after MEK treatment prior to rolling. a) Surface roughness vs. number of rolling. b) change in resistance vs. number of rolling.

Figure 20 Mechanical stability tests on PU layer assisted Ag based transparent electrode. a) Cyclic bending test for 1000 cycles (radius of curvature = 5 mm), and adhesion stability test by number of peeling using 3M scotch-tape.

Figure 21 PU layer assisted electro-mechanically stable Ag nanowire transparent electrode on diverse substrates. Demonstrating of lighting a

LED through the fabricated transparent conductors.

Figure 22 NWs directly embedded into PU film as a stretchable transparent strain-sensor.

Figure 23 a) Demonstration of SNU logo-shaped scalable display with a green fluorescence OLED having dimensions of 50 mm x 60 mm. b) IVL performance of the OLED.

Figure 24 Examples of kirigami structure in engineering applications

Figure 25 Schematic illustration of digital kirigami cutting process on ultra-thin/flexible NWs/cPI nanocomposite to fabricate various shaped stretchable transparent electrodes.

Figure 26 Kirigami patterning of NWs transparent conductor in various shapes. SEM images of various kirigami structures and their 2D designs in the insets: a) Uniaxial, b) Biaxial, and c) Square spiral (Scale bars are 200 μm). d) optical microscope (OM) image of AgNWs/cPI in biaxial kirigami pattern (on the left) and e) SEM images of AgNWs in the magnified blue box (on the right) (Scale bars are 200 μm and 50 μm respectively).

Figure 27 Optical properties of colorless polyimide (cPI), AgNWs/cPI nanocomposite transparent conductor and the transparent conductor with kirigami patterned in uniaxial pattern. Inset graph shows the relationship between electrical and optical properties of the pristine Ag nanowire based transparent electrode.

Figure 28 a-b) Stress-strain curves and simultaneously measured resistance changes as a function of strain for TKEs with short (red) and long (blue) cut, and without kirigami cut (black). Unit cell of uniaxial pattern and three key parameters of the unit cell in the inset. Actual cutting lines are marked as black lines.

Figure 29 a-c) Experimental stress-strain curves of varying kirigami geometries and d-f) corresponding electro-mechanical performance with the elongations. g) Specified geometries and kirigami parameters of L_c , x and y

for investigating mechanical behavior.

Figure 30 Cyclic bending test of TKE. Resistance changes versus the number of cyclic stretching of ITO/cPI electrode (black) and TKE (red) under the tensile strain of 400%. Magnified regional resistance change under cyclic stretching shown in the dashed blue box.

Figure 31 FEM images showing stress distribution of TKE with uniaxial pattern under various tensile strains and corresponding real images. Magnified FEM images of stress-concentrated region under each strain in the insets.

Figure 32 a) illustration of ablation process with Gaussian profile of laser beam. b) Edge effect on mechanical property of kirigami edge using ablation process.

Figure 33 Schematic illustration of uniaxial transparent kirigami heater (cutting dimensions: $L_c = 15$ mm, $x = 1.7$ mm, and $y = 1.7$ mm).

Figure 34 Wearable transparent kirigami heater that operates on the wrist at input voltage of 4.5 V and performs under dynamic movements (upward and downward).

Figure 35 a) Electrothermal and mechanical stability test verified by stretching under strain elongations of 0%, 50%, 100%, 150% and 200%. b) Maximum temperature at increasing input voltages from 1.5V to 9.0V. c) Cyclic operation temperature at 6 V. d) Resistance versus temperature of calculated and measured graph of transparent kirigami heater.

Figure 36 Configuration of transparent kirigami EP sensor for capturing various electrophysiology signals. The TKEs patterned as Ref., GND. and Mea. electrodes with the biaxial pattern and the additional thin Au coated layer at the skin contact.

Figure 37 Various electrophysiology signal measurements (locations and signals) for a) EMG, b) ECG and c) EOG. d) Schematic illustration of measurement locations on graphical human model for monitoring EEG

signal. e) EEG alpha rhythms observed at 10 Hz.

Figure 38 SNR comparison between conventional and TKE EMG signals.

Figure 39 Comparison of areal coverage and visibility between fractal, solid and kirigami electrodes.

Figure 40 a) Schematic illustration of skin-colored inhomogeneous elastomeric substrate for adhesion test. b) Stress distribution result of inhomogeneous elastomer when strain of 20% is applied. Adhesion test for c) pristine thin film versus d) kirigami thin film (scale bars are 3.5 cm).

Figure 41 Schematics of selective galvanic replacement gold (Au) coating process.

Figure 42 a) EDS image that shows Au layers coated selectively on the exposed surface of the AgNWs. i) SEM image, ii) Ag only, and iii) Au only. b) Oxidization stability test in thermally accelerated condition. c) Biocompatibility test via immersion in phosphate buffered solution (PBS) solution.

Figure 43 Flow diagram of human-machine interface using TKE.

Figure 44 Human-machine interface using transparent kirigami electrodes.

a) Two sets of measured sEMG signals from both forearms using TKE sensors. Roman numbers enclosed in the orange box under the RMS signals represent corresponding commands in c). b) Schematic illustration of demonstrating human-machine interface via TKEs by controlling a quadrotor with the gestures, which are signal processed by Bluetooth and WiFi-network. c) Description of control motions and corresponding gestures: i) Take off, ii) Fly forward, iii) Turn left, iv) Turn right, and v) Land.

Figure 45 (Left) Description of control motions and corresponding gestures: i) Take off, ii) Fly forward, iii) Turn left, iv) Turn right, and v) Land. (Right) The route of a quadrotor drone in HMI demonstration and its corresponding real images arranged as numbers in order.

Figure 46 Engineering structure of silver nanowires based transparent electrode for highly flexible / stretchable transparent electronics.

Chapter 1. Introduction

1.1. Study Background

Form of electronic devices are constantly changing and have had a societal impact to people, industry and daily lives. Especially, display and energy devices have brought the greatest change over only a few decades. However, transparent conductive layer, which is an essential layer for displays, is made out of fragile nature of ceramic material, indium tin oxide (ITO) or fluorine-doped tin oxide (FTO).

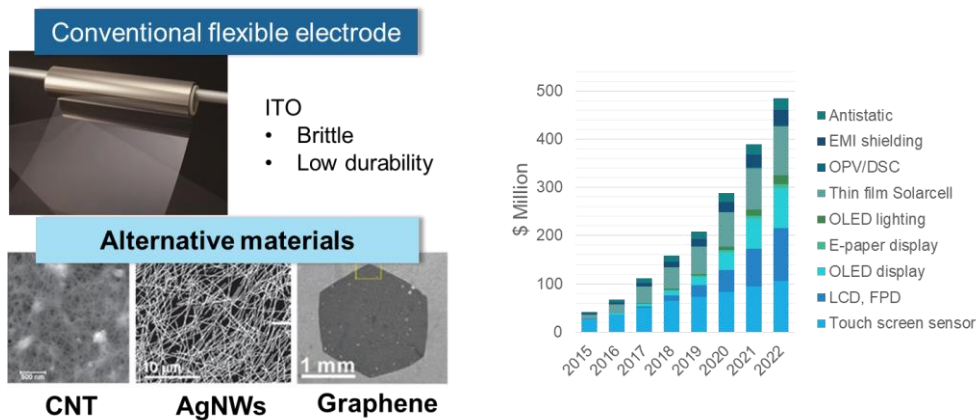


Figure 1 Growing need for alternative transparent electrodes as the form of electronics starting to change from rigid to flexible. Candidates for alternative to ITO are carbon nanotubes, silver nanowires (AgNWs) and graphene. Market speculation of transparent conductors by the products. (Right)

As a consequence, alternative transparent conducting materials for replacing the transparent anodic electrode has been greatly swept research

fields for a couple decades and is still on-going futuristic industry or another field that many industrial companies are interested in commercialization of alternative transparent conductive materials (**Figure 1**). Among the alternative materials, solution processable AgNWs are still one of the strongest candidate as a substitute for the conventional material due to their superior electrical, optical and mechanical properties.

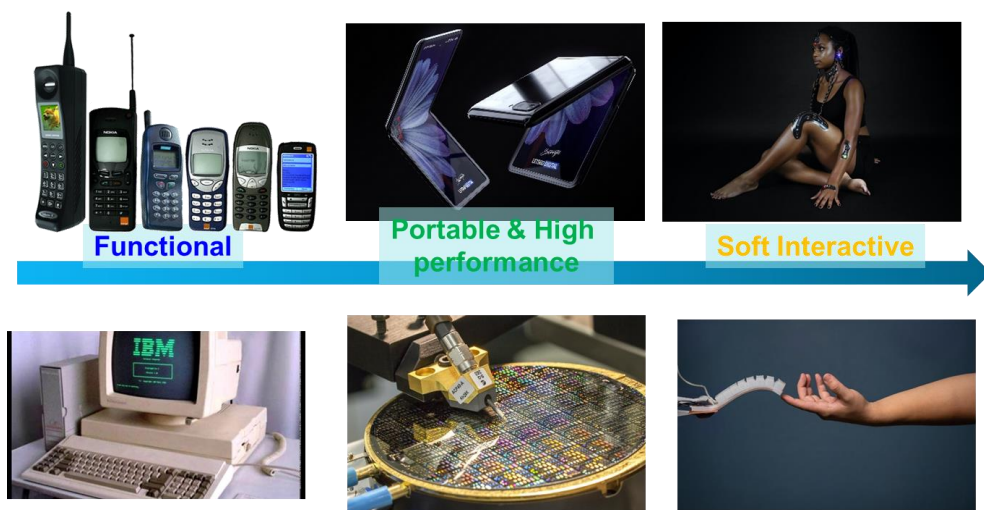


Figure 2 Electronics from the past to the future.

Furthermore, the future electronics beyond the hardships at present is speculated that it would not only be flexible but also stretchable, which can be interactive with human body (**Figure 2**). Such technologies typically developed with materials innovation, processing technology and modified design engineering. Efforts in developing these soft and stretchable electronic materials been largely focused on improving electrical and mechanical performance, including to achieve greater electrical conductivity,

stretchability and skin-like softness.

1.2. Purpose of Research

In this research, development of silver nanowire based transparent electrode is considered from understanding of synthesis level to engineering structural design at nano-micro-scales. By engineering at multi-scale dimensions, there are many opportunities of fabrication approach that could dramatically improve the performance of nanomaterials based conductor thereby knocking down obstacles that were present.

In my dissertation, I have proposed various structural engineering at nano / micro scales for fabrication of highly flexible / stretchable silver nanowire based electrode, in order to overcome electrical, mechanical optical properties that limit either its potentials or performances for wide-variety of applications.

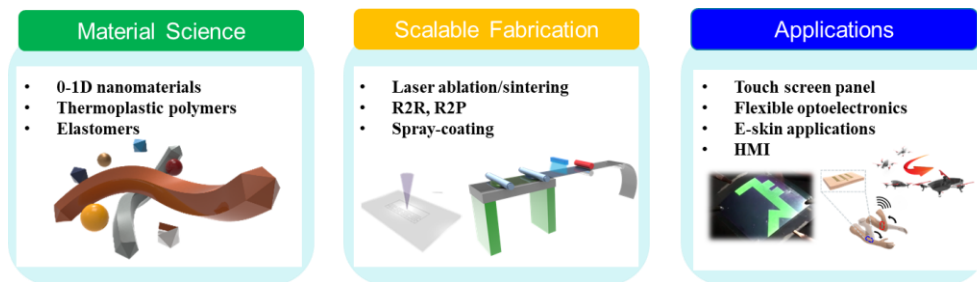


Figure 3 Research approaches for the development multifunctional high performance silver nanowire based flexible / stretchable transparent conductor.

First, instead of modification of molecular level of during the synthesis,

NWs with different dimensions that each have structural advantages both at nano-micro- scales have been employed to provide high quality transparent electrodes and demonstrated high performance display. For the second approach, a solution-based phenomenon from scalable fabrication approach that simultaneously solves mechanical, electrical and chemical stability that the nanowire based network conductor had ben suffered. This process has demonstrated to possess a lot of applicability, such as electronic textile (E-textile) or integration of soft robotic sensory system, since the process can be applied to diverse substrates. Lastly, a structural design approach has been proposed at the micro-scale to engineer AgNWs based transparent flexible conductor into elastic stretchable conductors. Therefore, it is expected that it would alleviate intrinsic mechanical hysteric behavior of 1-D nanomaterials and demonstrate a series of wearable applications that could not have been achieved without engineered softness, which are including stretchable heater, electrophysiology (EP) sensing electrodes and human-machine interface electronic-skin (E-skin).

Chapter 2. Fabrication of Highly flexible Ag nanowire based transparent electrode

2.1 Demand for Ag nanowire based transparent flexible electrode as an alternative to ITO.

Transparent electrodes, which are an essential component in current displays and touch screens markets, have commonly been made of indium tin oxide (ITO). Silver nanowires (AgNWs) have been developed for several decades and widely applied to optoelectronic devices as an alternative to the ITO transparent conductors.[1-4] Their characteristics such as yield, length and aspect ratio have been steadily improved by optimizing synthesis conditions as previously been discussed. Although carbon nanotubes (CNTs) and graphene are promising candidates as transparent conducting materials for optoelectronic devices,[5-7].

Touch screen panels with AgNW transparent electrodes have been widely demonstrated, and they show relatively high performance because of simplicity in fabrication compared to the other methods. However, application of AgNW percolation networks in thin film devices such as organic light emitting diodes (OLEDs) and energy devices remains very challenging due to relatively large surface roughness, reduced effective electrical area and poor adhesion to substrates. Overlaid multiple layers of AgNWs increase the surface roughness, and the dimples on the electrode usually cause highly non-uniform electrical currents, which results in the

interlayer shorting, high leakage currents, and low quantum efficiency in OLEDs. Additionally, poor adhesion to the substrates degrades the electrical and mechanical stability of the fabricated devices. Compared to AgNWs, CNTs, graphene and conducting polymer films have much smoother roughness with lower than 10 nm peak-to-valley values of roughness and large effective electrical areas due to its much smaller diameter, uniform thickness and two-dimensional property.

2.2 Dual-scale silver nanowires based transparent electrode

Commonly, the diameter of synthesized AgNWs is around tens of nanometers to hundred nanometers. Once a AgNW percolation network is formed, its roughness is at least tens of nanometers, and it increases more than twice in the NW junction parts. In order to fabricate high performance optoelectronic devices, many techniques to reduce the roughness of AgNW electrodes have been developed. Overcoating a AgNW network with a transparent conductive material such as PEDOT:PSS[8-11] or a buffer layer such as molybdenum oxide (MoO_3)[12] can effectively reduce the surface roughness. However, an excessively thick polymer layer may lead to an increased driving voltage and/or electron-hole imbalance, thus deteriorating the device performance.[13] Although recent demonstrations using AgNWs embedded in substrates may decrease the surface roughness below 10 nm without an overcoat layer, AgNWs are found to be immersed in substrates in some areas, reducing the effective electrode areas that are already smaller

than those of unpatterned thin-film electrodes.

2.2.1 Integration of silver nanowires at different length scales

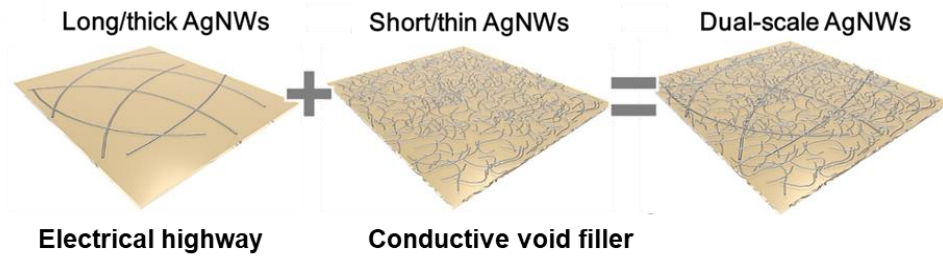


Figure 4 Concept of a dual-scale Ag nanowires based transparent electrode.

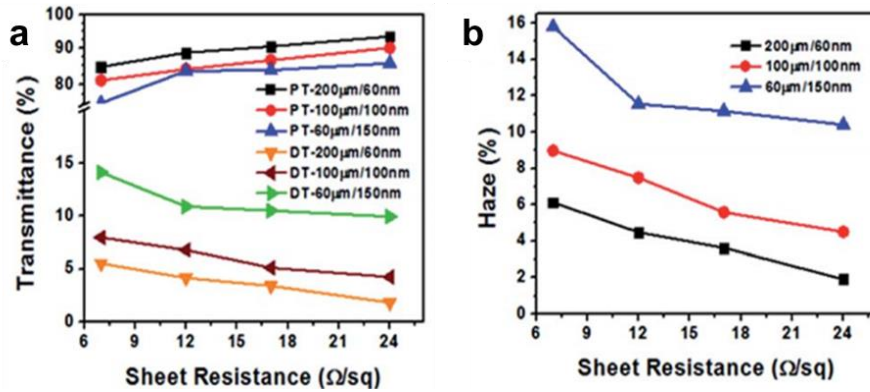


Figure 5 Optical properties of silver nanowires at different length and diameters. a) Transmittance vs sheet resistance, b) Haze vs. sheet resistance.

To overcome the current limitations of single-sized metal NW network-based transparent electrodes, a proof of concept of a dual-scale AgNW based electrode composed of AgNWs with two different length and diameter is schematically described in **Figure 4** and SEM images are taken in **Figure 6**. As shown in **Figure 5**, as the length and the thickness of nanowires are

long and smaller, the electrical and optical properties get maximized. However, the yield amount of such an approach to synthesize long / thin nanowire is low, it has been tackled by different approach.[14] By integrating a long/thick AgNW network as a backbone electrical highway for the carrier transport with a short/thin AgNW as a conductive filter network connecting long/thick AgNWs across large percolation (**Figure 6**).

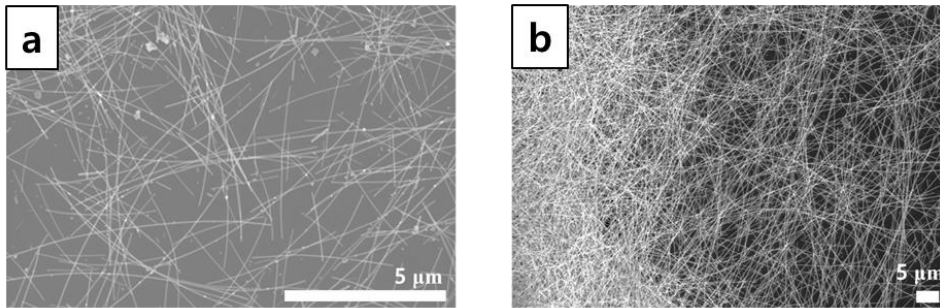


Figure 6 SEM pictures of synthesized a) short/thin AgNWs (10 μm / 40 nm) and b) long/thick AgNWs (100 μm / 100 nm).

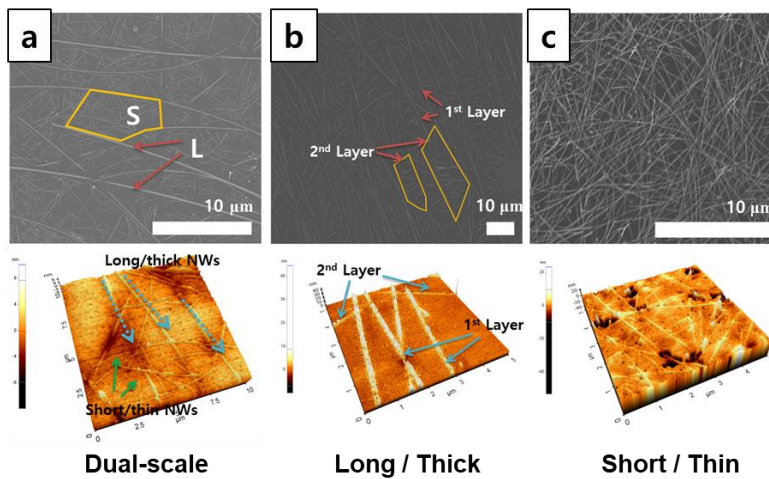


Figure 7 SEM and AFM images of fabricated silver nanowire based

transparent conductor (a) dual-scale NWs (b) long/thick NWs and (c) short/thin NWs.

The deposition of dual-scale AgNWs is advantageous because the secondary AgNW networks can be constructed on the voids formed between longer NW percolation network. The SEM images in **Figure 7b,c** actually show percolation network consisting of only long or short NWs while **Figure 7a** shows the dual-scale NW network of combination of short and long NWs. Atomic force microscope (AFM) (**Figure 7 a-c, bottom**). In case of short/thin AgNWs, however, it is confirmed that short/thin NWs that were in upper layers on the donor substrate, that is, NWs not in contact with the substrate surface but located on other NWs, are mostly deeply buried in the polymer after the peel-off, while higher density NWs are still needed to maintain similar sheet resistance compared to the long/thick NWs in terms of percolation theory. This signifies that only some short/thin NWs will directly contribute to the conduction. Therefore, the dual-scale NW network has a higher NW density, with the long/thick NWs as backbones and short/thin NWs as local branches connecting long/thick NWs. Additionally, the number of exposed NWs was increased even though the same amount of NWs were deposited, thereby achieving high transparency and low sheet resistance.

Surface Coverage of dual scale nanowires

Calculation of surface coverage regarding 1-dimensional network film

has been adapted from Wiley Group.[15] In this report, coverage A_c was calculated by the following equation.

$$\%T = 100 - 87A_c \text{ (eq. 1)}$$

This equation is related to transmittance of fabricated electrodes without diameter of nanostructures. Based on this equation, calculated coverage are 0.057, 0.086 and 0.0919 for each long / short / and dual scale NWs respectively. Higher value means larger coverage. Calculated areas of voids in percolation network are $\sim 7 \mu\text{m}^2$, $\sim 1 \mu\text{m}^2$ and $\sim 5 \mu\text{m}^2$ for each long/short/ and dual scale. It clearly means that adding short/thin AgNWs into larger network can reduce the size of voids and increase the coverage. However, although percolation network consisting of short/thin AgNWs has smaller voids compared to others, its increased number of junctions disturbs the current spreading and makes surface rough in the electrode. Thus, dual-scale NWs network is employed to minimize shorts and to provide moderate coverage.

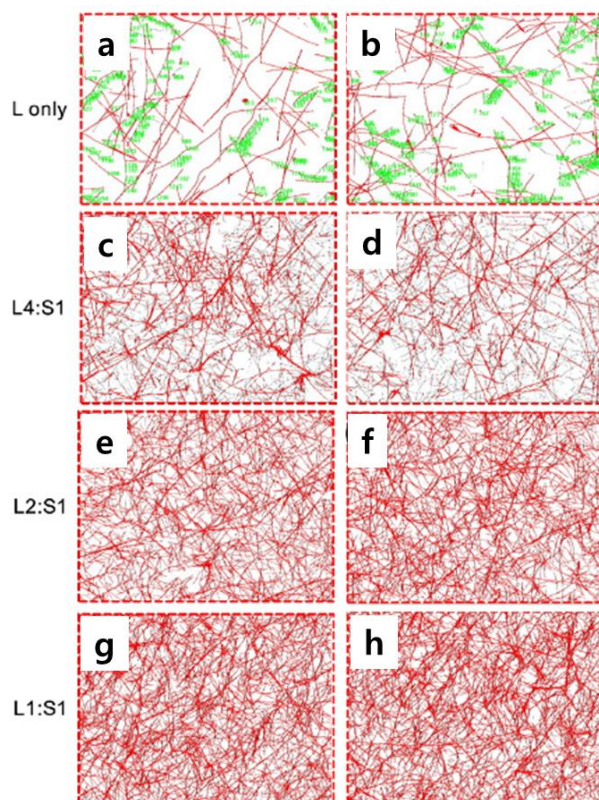


Figure 8 Transformed and counted SEM images based on different coating ratio by segmentation in Image Pro.

In addition, its coverage also has been measured by image analysis tool. As shown in **Figure 8**, SEM images are transferred to black-and-white images by segmentation in Image Pro and counted based on pixels. Although coverages are different, each sample has same sheet resistance (50ohm/sq). Surface coverage (L1:S1 ratio) is increased in dual scale compared to electrode based on long AgNWs.

Surface roughness of dual NW based transparent electrode after embedding

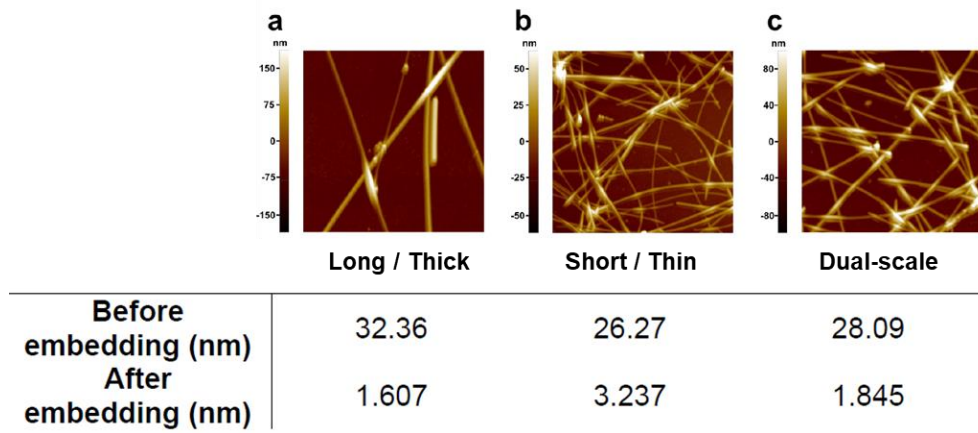


Figure 9 AFM topography of AgNWs network before embedding a) long/thick AgNWs b) short/thin AgNWs c) dual-scale AgNWs and corresponding roughness before/after embedding.

The AFM analysis has been performed for AgNWs deposited onto glass substrate which is prior state to embedding process. **Figure 9** shows difference in coverage according to types of AgNWs. RMS values of the long, short and dual AgNWs are 32.36nm, 26.27nm and 28.09nm respectively. RMS values decreased conspicuously through burying of AgNWs. Interestingly, RMS of short AgNWs is lowest among the electrode before embedding process but RMS of long and dual AgNWs is approximately twice smaller than that of short AgNWs after embedding process. While long AgNWs are buried in UV resin well, short AgNWs are too thin to be held. Long AgNWs can also hold short AgNWs not to be

detached from surface in dual AgNWs network.

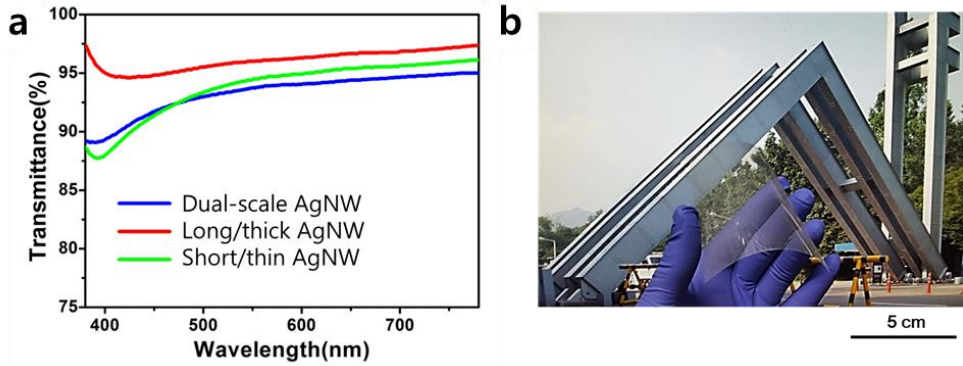


Figure 10 a) Spectral transmittance of dual-scale AgNWs (blue), long/thick AgNWs (red) and short/thin AgNWs (green). b) Digital image of a transparent conductor using dual-scale AgNWs.

Therefore, the fabricated dual-scale AgNW network transparent conductor is composed of two different sized AgNWs. Long/thick AgNWs provide efficient pathways for the charge carrier transport in spite of lower transmittance. Short/thin AgNWs connect the long/thick NWs to further enhance the transmittance and electrical conductivity of the dual-scale NW network. By integrating a long/thick AgNW network as a backbone highway for the carrier transport with a short/thin AgNW network connecting long/thick AgNWs across large percolation voids, the fabricated dual-scale AgNW network transparent conductor showed superior optical and electrical characteristics suitable for flexible optoelectronics [16-18] with over 90% transmittance in a broad spectral region and low sheet resistance (50 Ohm/sq.) (**Figure 10**).

Stability of the embedded transparent electrode

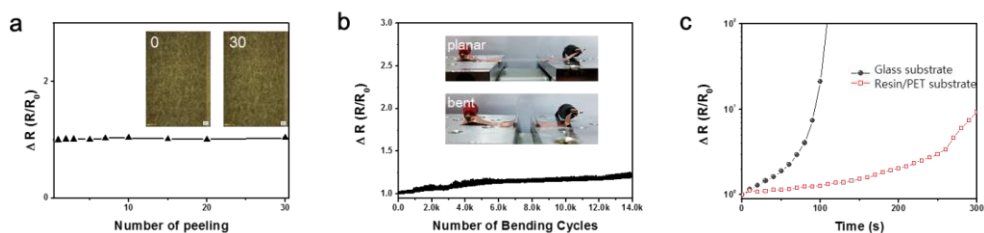


Figure 11 Stability of the embedded dual-scale AgNWs based transparent electrode. a) Adhesion test by tape test, b) mechanical stability test by cyclic bending and c) chemical stability test in an air plasma environment.

In addition, by constantly measuring the resistance of electrode, it had been demonstrated adhesion stability under 30 times of peel-off test (**Figure 11a**) and high mechanical stability even later 14,000 times of cyclic bending test (**Figure 11b**). Moreover, it was found that the oxidation stability is increased by UV curable polymer encapsulation. Silver has a better oxidation stability compared to copper or aluminum.[16] However, oxidation of silver is also accelerated when size is shrunk to the nanoscale due to large surface area. By applying air plasma treatment, which excites gas atoms with higher energy state, the oxidation resistant characteristics of the AgNW electrode have been investigated with and without the UV curable polymer encapsulation. **Figure 11c** shows the transient electrical resistance change, comparing the oxidation stability of the bare AgNWs on a glass substrate and the embedded AgNW network on a flexible substrate during air plasma treatment.

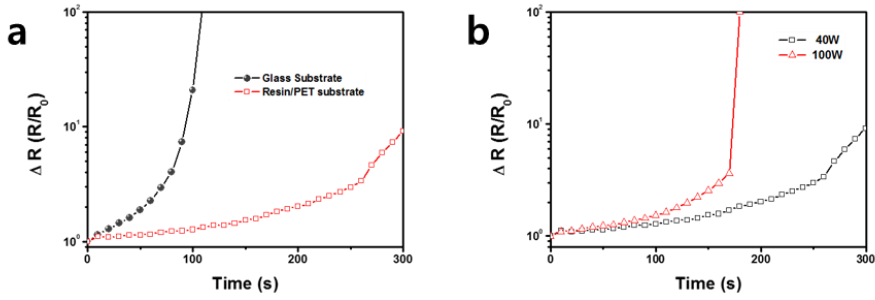


Figure 12 a) UV resistant test of embedded NWs versus NWs on a bare glass substrate under 40 W plasma treatment. b) UV failure test of embedded NWs under 40 and 1000 W plasma power treatment condition.

Although the changes in resistance (R/R_0) values of the embedded AgNW network increases depending on plasma power and time (**Figure 12**), the embedded AgNWs network showed much more enhanced oxidation stability compared to the bare AgNWs network on a glass substrate. This is because encapsulation of the AgNW network with a UV curable resin minimizes the direct NW exposure to the environment and reduces the oxidation problem, with only the bottom surface of NWs in contact with the donor substrate before the peel-off being exposed on the surface of the flexible substrate. Since total encapsulation of the AgNW would decrease the surface conductivity, the optimum exposure of the AgNW on the surface is needed to achieve low sheet resistance while maintaining superior oxidation stability and transparency at the same time.

2.2.2 Dual-scale Ag nanowire based transparent electrode as organic light emitting diode (OLED) application

To verify the effect of dual-scale integration, a flexible phosphorescent OLED is fabricated, where a dual-scale AgNW network was employed as a transparent anode, and its characteristics were compared with OLEDs whose anodes were made of single sized AgNWs (only long/thick AgNWs or only short/thin AgNW).

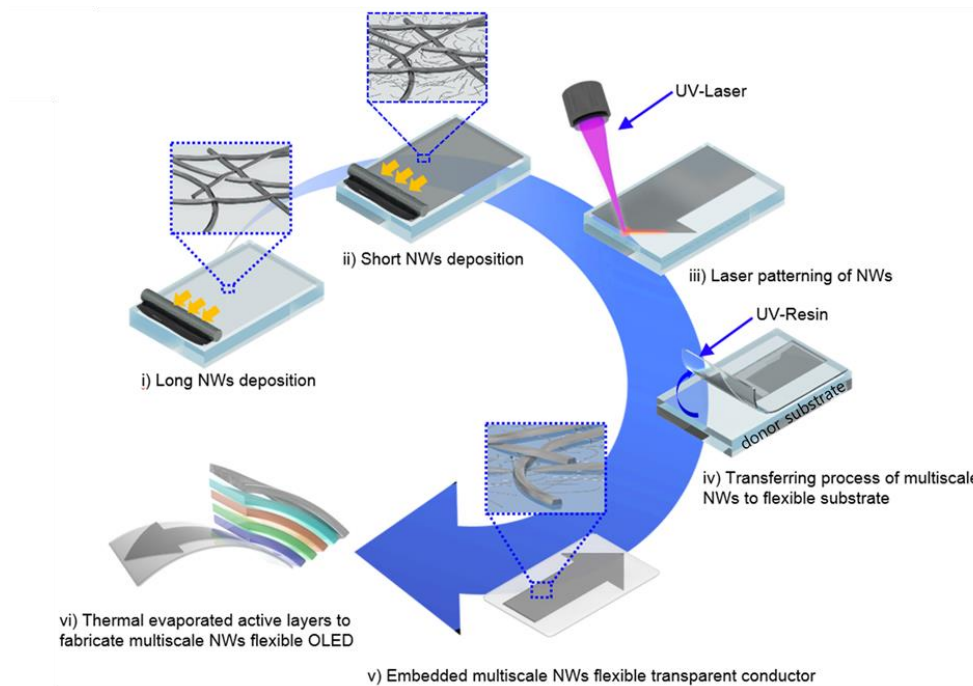


Figure 13 Illustration of dual-scale AgNW network transparent conductor fabrication process and its application for flexible OLED demonstration.

The fabrication process of dual-scale AgNW network transparent electrode preparation and patterning for a flexible OLED demonstration is illustrated in **Figure 13**. The dual-scale AgNW network transparent

conductor is obtained by successive depositions of two different sized AgNWs; relatively longer and larger diameter (100 μm / 100 nm) AgNWs followed by shorter and smaller diameter (10 μm / 40 nm) AgNWs. Dual-scale AgNWs were synthesized via precise control of synthesis condition and morphology of AgNWs such as length and diameter [19, 20] and were coated on a glass substrate to make the dual-scale network. After dual-scale NW network deposition, the transparent conductors were patterned by a direct laser ablation for arbitrary transparent conductor patterning. The patterned dual-scale AgNW network transparent conductor was then transferred to a flexible substrate by embedding the transparent conductor film into a UV curable resin[21, 22], which further enhances the adhesion, surface roughness and mechanical robustness of the conductor film. Large area transparent conductor films can be made by a bar-coating method that spreads out AgNWs in solution phase.

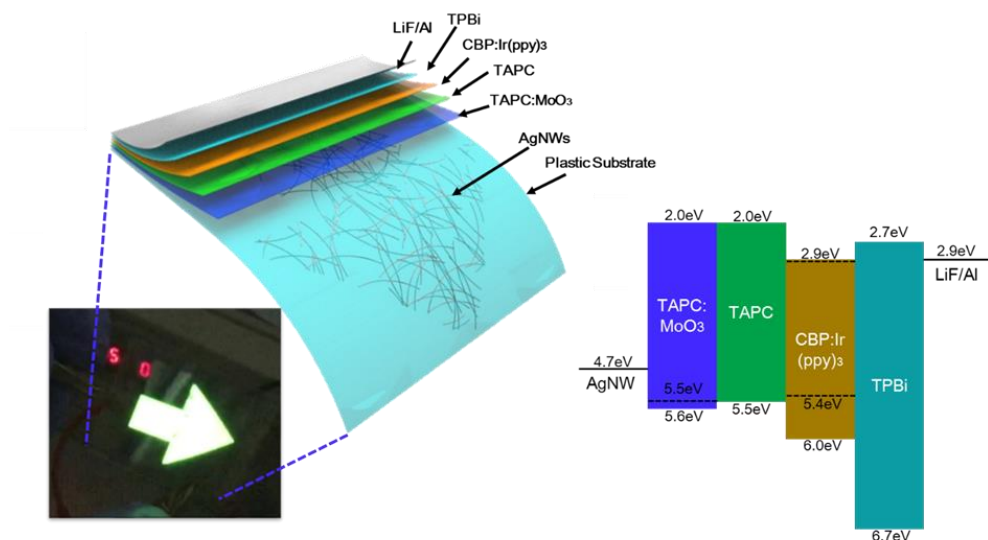


Figure 14 Schematic illustration of the OLED layers along with a digital image and energy diagram of OLED structure.

The structure of an arrow shaped OLED layers shown in **Figure 14**, including the emissive layer composed of 4,4'-N,N-dicarbazolbiphenyl (CBP) doped with fac-tris (2-phenylpyridine) iridium (III) [Ir(ppy)₃], were deposited by thermal evaporation on plastic substrates coated with AgNW networks, as described in the Experimental section.

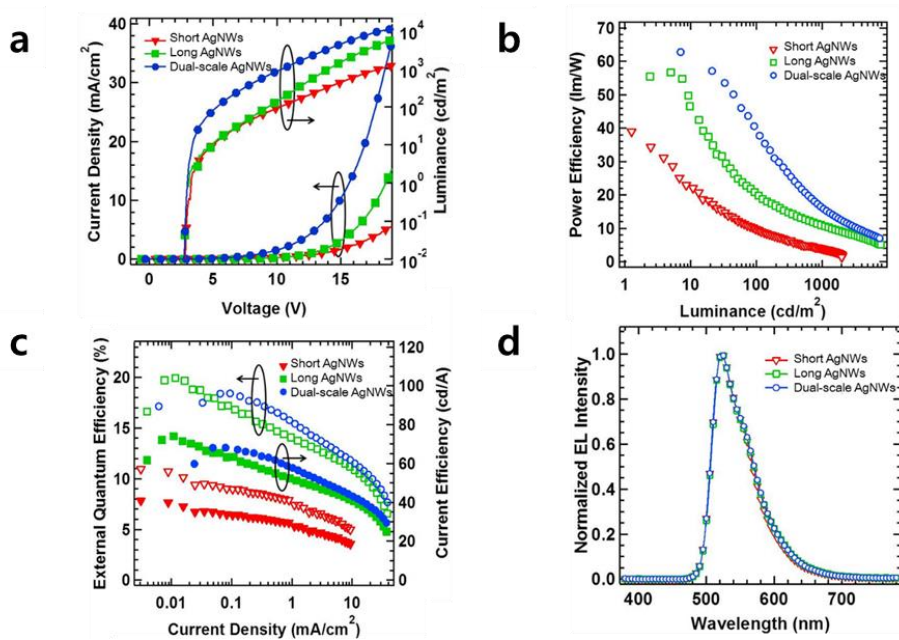


Figure 15 OLED characterization in (a) current density and luminance, (b) power efficiency, (c) external quantum efficiency (hollow symbols) and current efficiency (solid symbols) and (d) normalized electroluminescence spectra (at the current density of 25mA/cm²) from OLEDs using three different types of AgNW network transparent conductors (short AgNWs, long AgNWs, dual-scale AgNWs).

The current density vs voltage (J–V) characteristics show that at a given V, the values for J of the three devices are very differently, with an order of increase in J from the short/thin AgNW, the long/thick AgNW, to the dual-scale AgNW OLED. This is attributed to the difference in the effective device area A_{eff} , arising from the difference in the total exposed area of a AgNW network – the sum of AgNW areas that are not covered with the

polymer resin prior to the OLED deposition – which is found to be much larger for the dual-scale AgNW network than for the single sized AgNW network, as confirmed by the AFM characterizations. As a result, at a given V the total current I passing through the dual-scale AgNW OLED (blue circles, **Figure 15a**) is much larger than that through the single sized AgNW OLED (red circles for short AgNWs and green circles for long AgNWs, **Figure 15a**). Since J in **Figure 15a** is obtained by dividing I by the geometrical device area (A_{geo}), which is determined by the overlap of the cathode and the anode and hence is the same for all three cases, J of the dual-scale AgNW OLED is much larger than that for the other devices over the entire range of V .

The different degrees of discrepancy between A_{eff} and A_{geo} for the three devices can also explain the major features of the other characteristics shown in **Figure 15a-c**. Since the luminance L increases with I , L at a given V in the L – V characteristics (**Figure 15a**) is largest for the dual-scale AgNW OLED, with the order of increasing L equaling that of increasing J in the J – V characteristics. The external quantum efficiency (EQE) and current efficiency (CE) of Ir(ppy)₃-based phosphorescent OLEDs are known to decrease with increasing J due to the concomitant increase in charge imbalance and nonradiative exciton quenching.[23] Since the local densities of charges and excitons in the emissive layer, which determine the degree of efficiency roll off, decrease with increasing A_{eff} at a given J , the

EQE and the CE of the dual-scale AgNW OLED are largest with respective maxima being 18.7 % and 68.6 cd/A, while those of the short/thin AgNW OLEDs are smallest (**Figure 15b**). From the L–V and EQE–J characteristics, it is seen that the values of V and J required to produce a same level of L are smaller for the dual-scale AgNW OLED than those for the other devices with single sized AgNWs. In addition, the EQE at that operating point is also highest for the dual-scale AgNW OLED. As a result, compared to the short/thin or long/thick AgNW OLEDs, the dual-scale AgNW OLED has the highest power efficiency (PE) over the entire range of L, with a maximum of 62.8 lm/W (**Figure 15c**). Electroluminescence spectra of the AgNW OLEDs measured at $J = 2.5 \text{ mA/cm}^2$ resemble the shape of typical Ir(ppy)₃ electrophosphorescence and are almost identical to one another, meaning that the optical properties of the weak microcavity OLEDs are mostly not affected by the transparent, randomly distributed AgNW networks (**Figure 15d**).

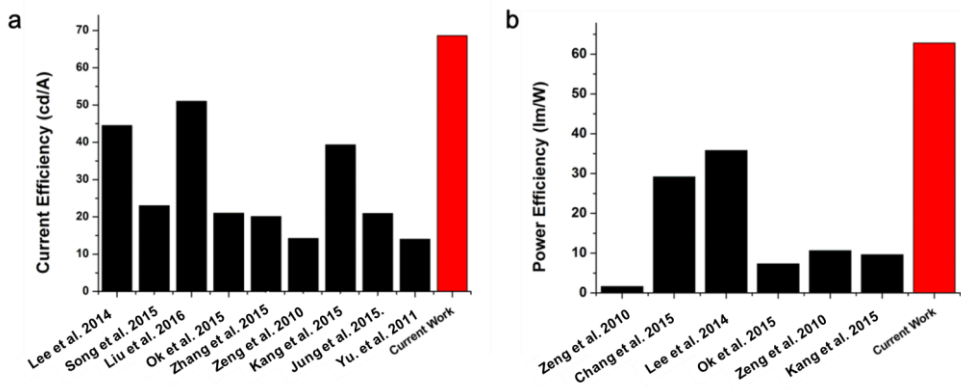


Figure 16 a) Current efficiency and b) power efficiency comparisons (black bars: previous OLED with a single sized AgNW transparent electrode, red bars: current work with a dual-scale AgNW transparent electrode).[24-33]

Figure 16 shows that the CE and the PE of the dual-scale AgNW OLED are superior to those of OLEDs with single scaled AgNW electrodes that have previously reported, demonstrating that the dual-scale AgNW network transparent conductor has great potential for use in flexible, high performance optoelectronic devices.

2.2.3 Experimental section for dual-scale NW transparent electrode

Synthesis of short/thin AgNWs: In this experiment, relatively short (10 μm) and small diameter (40 nm) AgNWs were synthesized by a glycerol-based polyol method. First, the mixture of two different PVPs, $M_w \sim 360,000$ and $M_w \sim 40,000$ with weights of 0.2 g and 0.8 g, respectively, were dissolved in 100 mL glycerol. In a separate vial, 5 mL glycerol solution containing 0.0076 g of sodium chloride is prepared in a warm condition. 0.3 g of silver nitrate (AgNO_3) was thoroughly dissolved in 600 μL of DI water. These freshly-made NaCl solution and AgNO_3 solution were sequentially poured into the prepared PVP solution in a flask. The solution was then stirred using a magnetic stirrer for 1 min, and it was placed in a preheated oil bath at 130 $^\circ\text{C}$ for the growth of NWs. The reaction was sustained for 3 hr. Once the synthesis of AgNWs was completed, the AgNWs solution was

washed with methanol at v/v 8:1 ratio with centrifugation at 5000 rpm for 10 min three to four times. Then, the cleaned short AgNWs were dispersed in IPA to be ready for the use.

Synthesis of long/thick AgNWs: In order to synthesize relatively long (100 μm) and large diameter (100 nm) AgNWs, the amounts of all reagent chemicals involved in previously introduced polyol method had to be precisely controlled. However, this typical synthesis employed a one-pot process, where all reagents are dumped into a tri-angular flask at once, thus offering a facile and simple synthesis of long nanowires. In 50 mL of ethylene glycol (EG), 0.4 g of PVP ($M_w \sim 360,000$) and 0.5 g of silver nitrate (AgNO_3) was sequentially dissolved using a magnetic stirrer. Once thorough dissolution of all solutes was achieved, the stirrer was carefully removed from the mixture solution. Then, 800 μL of $\text{CuCl}_2 \cdot 2\text{H}_2\text{O}$ (3.3 mM) was rapidly injected into the mixture and stirred mildly with a hand for 1 min. Finally, the mixture solution was suspended in a preheated silicone oil bath at 130 $^\circ\text{C}$. The growth of AgNWs in the mixture was maintained at the elevated temperature for 3 hr. The resultant solution was then cleaned using acetone and ethanol to remove the chemical residues along with centrifugation of 3000 rpm for 10 min for three to four times. The purified AgNWs were re-dispersed in 1-propanol (IPA) for the use.

Fabrication of a dual-scale AgNWs based transparent electrode: In fabricating dual-scale AgNWs based transparent electrode, Meyer rod

utilized bar-coating method was used. To avoid aggregation of the NWs during the NWs dispersion via bar-coating process, the coating process was conducted on a heated glass substrate to induce rapid vaporization of the NWs solvent while maintaining uniform and thin layer of conducting film. The transparent electrode exhibiting low sheet resistance $< 50 \text{ } \Omega/\text{sq.}$ was achieved by stacking multi-layers of the NWs solution in longitudinal and transversal directions several times on the targeted substrate. Thus, both types of NWs followed the same procedure for the dual-scale transparent electrode preparation.

Transferring to flexible substrates: The transparent electrode could be easily transferred from glass donor substrates to flexible substrates with a curing and peel-off method. First, commercially available epoxy resin (SEA-1) with moderate amount was put on top of the donor substrate. Using Meyer rod, liquid epoxy resin was uniformly spread on the patterned donor substrate and then cured using an ultraviolet light lamp (KJUV, KCHS04) for 90s (with 1kW power and 254 nm wavelength), and was easily peeled off from the rigid donor substrate along with the patterned AgNWs structure and flexible PET film.

2.3. Contact resistance of nanowire to nanowire

Silver nanowire (AgNW) based transparent electrode often challenged by high NW to NW contact resistance and poor long-term chemical and mechanical stability due to poor interface between NWs and the substrate.

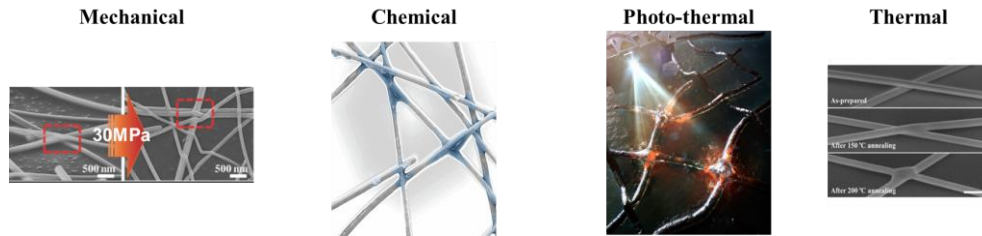


Figure 17 Proposed welding approaches for NW contact resistant improvements. [34-37]

Even though there are many number of approaches that have shown improvement in electrical properties (**Figure 17**), these still lack either mechanical stability or long-term stability due to high areal exposure time of NWs or mismatched heterogeneous interface that chemical degradation occurs. Therefore, there have been extensively researched not only on the welding process but also embedding process. However, embedding and welding could not have been achieved in a single step for many of proposed approaches.

2.3.1 Room temperature fabrication of Ag nanowire based high performance transparent electrode

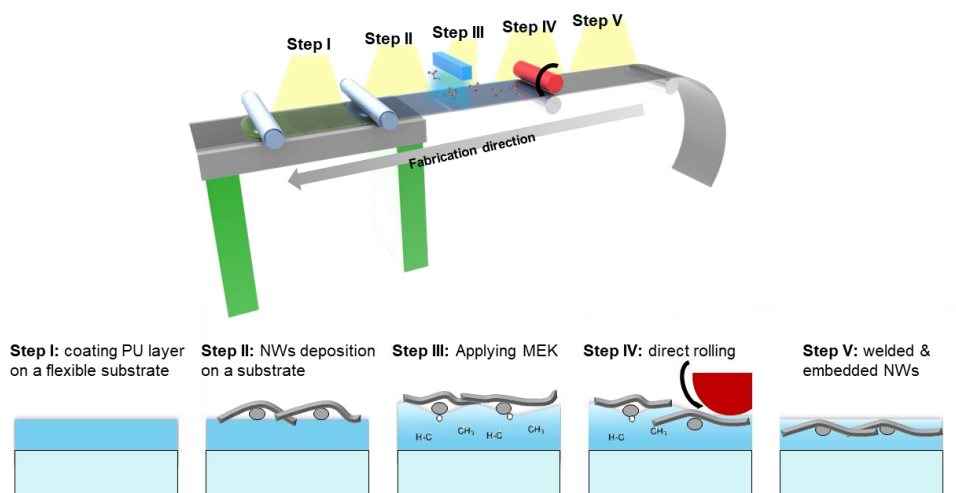


Figure 18 Steps that undergoes for a swellable polymer layer assistive welding / embedding at room temperature.

Herein, a room temperature direct welding and chemical / mechanical protection strategy is achieved by coating a thin layer of polymer, which is highly swellable to specific wet chemical solvent, to join NWs together by a simply rolling process thereby greatly improving the conductivity and stability of the AgNW based transparent electrode (**Figure 18**). Specifically, 2-butanone (MEK) solution is treated over the surface of polyurethane layer, making highly swollen so that making spaces for NWs to be embedded if a firm mechanical pressure like smooth rolling is applied, thus allowing the NWs to be embedded in PU matrix and tightly joining together at room temperature. This technique may be most efficient in a manner that other

approaches achieve similar performance by thermal, chemical and mechanical treatment to the NWs.[38]

2.3.2 Effect of PU layer on the performance of Ag nanowire based flexible transparent electrode

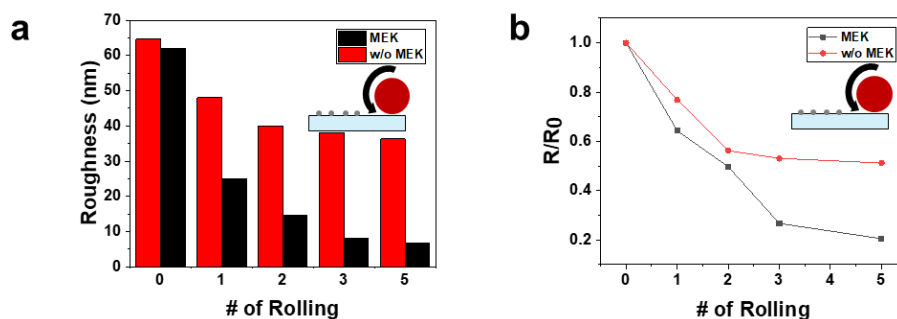


Figure 19 Effect of rolling before/after MEK treatment prior to rolling. a) Surface roughness vs. number of rolling. b) The change in resistance vs. number of rolling.

To examine the effect of swelling induced room temperature welding / embedding, the surface roughness is measured using atomic force microscopy (AFM) and electrical resistance after different number of rolling applied to the electrode (**Figure 19**). Once mechanical rolling pushes down the roughness of NWs, it has shown that the resistance significant drops up until one fifth of initial resistance after six number of rolling.

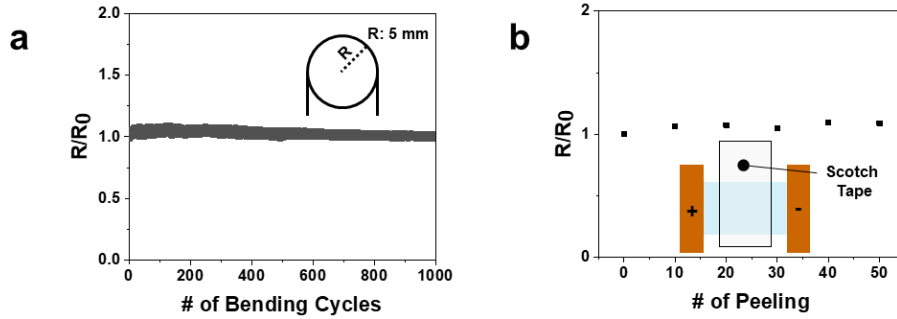


Figure 20 Mechanical stability tests on PU layer assisted Ag based transparent electrode. a) Cyclic bending test for 1000 cycles (radius of curvature = 5 mm), and adhesion stability test by number of peeling using 3M scotch-tape.

Mechanical stability of mechanically welded / embedded conductor is tested by cyclic bending test for 1000 cycles and adhesion stability under 50 times of peel-off test (**Figure 20**). The R/R_0 value after both tests have shown to be negligibly changed, so the mechanical stability is confirmed to be very excellent.

2.3.3 Coating of NW based transparent conductor on diverse substrates

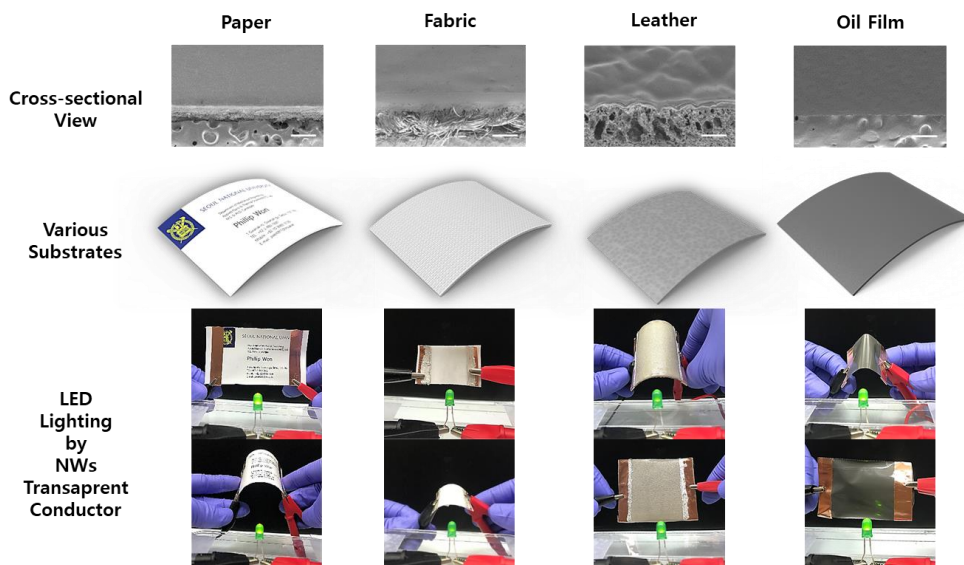


Figure 21 PU layer assisted electro-mechanically stable Ag nanowire transparent electrode on diverse substrates. Demonstrating of lighting a LED through the fabricated transparent conductors.

Interestingly, it has been found that by coating a thin layer of PU, it was able to form a nanowire based transparent conductor on diverse substrates. Here, coating procedure has been performed to different kind of substrates including paper, fabric, leather and oil film. There may be difference in their roughness without the PU layer but once PU solution gets penetrated inside those substrate and form a layer, it could have still act as adhesion media for coating Ag nanowires. Therefore, demonstration of lighting a LED has shown for all the transparent conductive surface substrates (**Figure 21**).

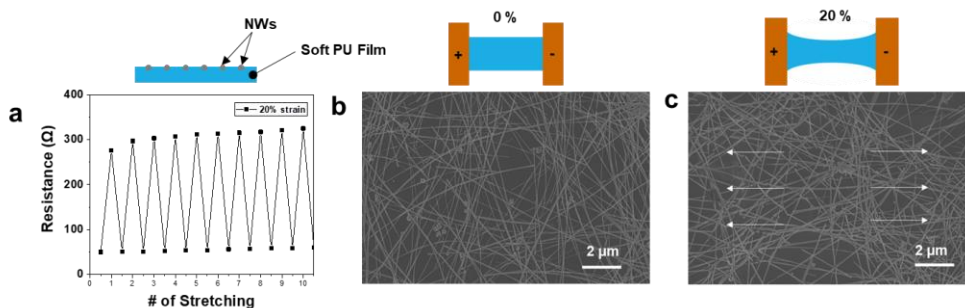


Figure 22 NWs directly embedded into PU film as a stretchable transparent strain-sensor.

In addition to the coated PU layer, this process was also applicable to a pristine PU film. Using the same approach, transparent NWs percolation strain sensor having gauge factor of 25 is fabricated (**Figure 22**). Transparent conductors in percolation system can induce the change in resistance arises from the contact resistance at each crosslinked joints, which can vary with deformations (Figure 18). These sensors are often well-suited for wearable devices and can be used to determine spatial position and joint angles as well.[39]

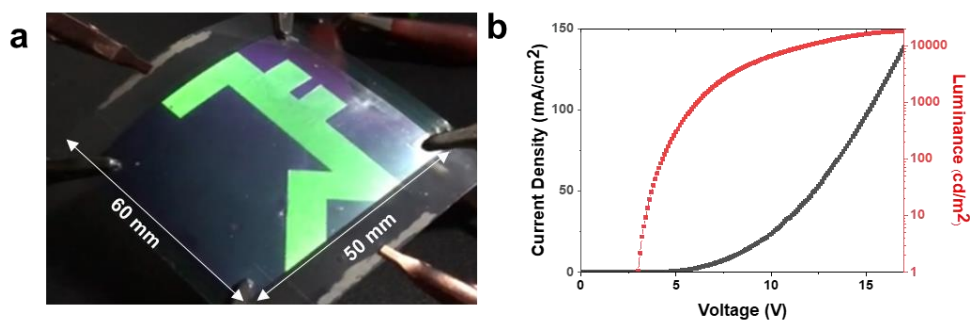


Figure 23 a) Demonstration of SNU logo-shaped scalable display with a

green fluorescence OLED having dimensions of 50 mm x 60 mm. b) IVL performance of the OLED.

Furthermore, similar to the previous OLED demonstration with dual-scale NWs electrode, the same device architecture has been constructed on PU layer assisted transparent electrode. It has shown IVL behavior that is comparable to the previous result with NWs based transparent conductor (Figure 23).

2.3.4 Experimental section for room-temperature post-treatment for high performance AgNWs transparent electrode

Coating of a swellable polyurethane layer: Water-based polyurethane dispersion, NPC-3600 (Nanux), is spin-coated to the substrates that NWs will be deposited. The coating recipe has three incremental spin-coating steps: 1. 300 RPM for 10 sec, 2. 1500 RPM, 30 sec and 3. 2000 RPM for 10 sec. After running the spin-coating recipe, the substrate is dried in an oven at 60 °C for 5 min to cure the PU layer.

Room temperature welding / embedding approach: First of all, long NWs that have been demonstrated are used in this experiment. For a substrate size 75 mm x 50 mm, 200 nanowires. In fabricating dual-scale AgNWs based transparent electrode, Meyer rod utilized bar-coating method was used. To avoid aggregation of the NWs during the NWs dispersion via bar-coating process, the coating process was conducted on a heated glass substrate to

induce rapid vaporization of the NWs solvent while maintaining uniform and thin layer of conducting film. The transparent electrode exhibiting low sheet resistance $< 50 \text{ } \Omega/\text{sq.}$ was achieved by stacking multi-layers of the NWs solution in longitudinal and transversal directions several times on the targeted substrate. Thus, both types of NWs followed the same procedure for the dual-scale transparent electrode preparation.

2.4 Fabrication of organic light emitting diode (OLED) using NWs based transparent electrode

Direct patterning of transparent electrode for OLED: Laser ablation of AgNWs electrodes has many advantages such as rapid process and fine resolution compared to the wet etching process.[39] This process offers handy computer aided design patterning particularly suitable for the ablation of NWs. Therefore, the mask-less laser ablation process is adopted for desire OLED patterning which have an arrow mark pattern with 5 cm x 2.5 cm large-size for a dual-scale transparent electrode. High repetition pulsed ns UV laser (InnoLas) at 30 KHz repetition rate with the average power of 50 mW is utilized as the ablation source. For the rapid micro-patterning, laser beam is focused by a tele-centric lens (Linos, $f=100 \text{ mm}$) while it is steered by a Galvano-mirror scanner (hurrySCAN II). Ablation pattern is easily altered by changing the associated CAD file, and the full design for the OLED application is attached as the supplementary figure. For a typical experiment, the scanning speed and the hatch size have been fixed to be

50mm/s and 500 μ m respectively. Due to the low ablation threshold of metal NWs, it is observable that the AgNWs are selectively removed from the surface without causing any noticeable damage on the substrate.

Flexible OLED fabrication: The same Flexible OLEDs were fabricated on transferred AgNWs substrates using vacuum thermal evaporation. The device structure was: PET / AgNWs:resin / 150 nm hole injection layer (HIL) / 20 nm hole transport layer (HTL) / 30 nm CBP:Ir(ppy)₃ / 40 nm electron transport layer (ETL) / 0.5 nm LiF / 100 nm Al. The HIL and HTL are composed of 1,1-bis[(di-4-tolylamino)phenyl]-cyclohexane (TAPC) doped with molybdenum trioxide (MoO₃), with a doping ratio of 25 vol %, and TAPC, respectively. The ETL is composed of 1,3,5-tris(N-phenylbenzimidazole-2-yl)benzene (TPBi). All organic materials for the fabrication were purchased from commercial companies.

2.5 Conclusion

In this chapter, fabrication based engineering approaches are utilized to fabricate silver nanowire based flexible conductor. First, by considering the optical and electrical advantages of the AgNWs at two different lengths/diameters, a dual-scale AgNW based flexible transparent electrode by assembling these two different sized AgNWs for the application developed in a highly efficient flexible phosphorescent OLED. Fabricated dual-scale AgNWs network transparent conductors have shown higher transparency with lower sheet resistance. In addition, the effective electrical

area of the fabricated electrode is increased by adopting dual-scale AgNWs and assigning most structure into the first layer while maintaining optoelectrical performance as transparent conductor. Therefore, efficiencies of a flexible OLED based on the dual-scale AgNWs electrode has been significantly increased compared to OLEDs with single sized AgNWs. Second, both welding and embedding processes typically required for Ag nanowire based transparent conductor could have been simplified by coating a swellable polyurethane polymer layer onto a substrate. This polymeric layer instantaneously get swollen upon treatment with chemical solvent thereby allowing NWs to penetrate into the polymer matrix in the swollen state simply by rolling process at room temperature so that NWs could remain at the surface of electrode. Therefore, both synthesis and fabrication based engineering approach enable the fabrication of highly flexible Ag nanowire based transparent electrode.

Chapter 3. Design engineering for Ag nanowire based transparent stretchable electrode

3.1 Background

In order to relieve discomfort between electronics and human body, fabrications of electrodes for stretchable circuits and devices has been approached by serpentine designs, ultra-thin films and extraordinary properties of nanomaterials to address the problems. Electronic-skin (E-Skin) that can detect and monitor bio-potentials while having conformal integration onto the skin is a desired form of delivering mechanical/electrical stimulus into quantitative electrical signals[40], and its investigations are extensively on-going for human machine interface (HMI)[41], soft robotics[42, 43] and continuous personal healthcare monitoring system in the field of ICT/IoT[41, 44, 45]. However, these strategies addressed thus far each face own limitation for achieving desired form of electronic-skin applications.

Two essential characteristics, conformability and imperceptibility (or transparency), are crucial when developing E-Skin to provide non-invasive precise monitoring of bio-signals directly from the surface of skin[46] and to look imperceptible to human-naked eyes in forms of a tattoo[47], a bandage[48] and a skin-replacement[49-53]. However, achieving stretchability and transparency simultaneously in high tensile strain (>50%) without degradation of electrical and mechanical properties is currently very

challenging. Although investigations of structural design to grant stretchability in flexible electronics have been widely demonstrated by serpentine or horseshoe structure[54], making appropriate structure to avoid generation of large or irreversible cracks in certain strain region (usually falls within 20~50%) is only achieved[47, 55-57]. Nevertheless, transparency and electrical conductivity is limited. Thus, with increasing demands of multi-functional wearable devices including display, energy generator/storage devices, various sensors and actuators[46, 58-65], E-skin devices must comprise characteristics that are mechanically stable under large tensile strain ($>50\%$) and transparent at the same time to realize vast range of applications[66-70].

3.2 Kirigami structure for engineering applications

Kirigami art, which is originally served as a ancient papercraft technique, also provides the way of shaping functional hierarchical structures for various engineering applications, for example, stretchable energy devices, wearable sensors, and self-folding scaffolds with tissue engineering, etc. The techniques based on kirigami concept involve cutting of substrates to provide a wide range of applications in different length scale from meter to micro/nanometer size.

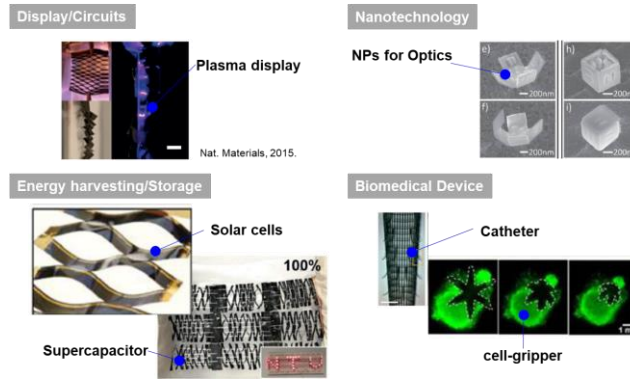


Figure 24 Examples of kirigami structure in engineering applications.

This simple but unique technique realizes facile and easily accessible modulation of material for mechanical, electrical, and optical properties. Furthermore, development of various kirigami fabrication processes in previous researches has a vast range of material choices, from familiar materials like paper, fabric and metal sheets to advanced materials such as 2D materials and nanocomposites, by introducing computer-aided cutting, lithography/etching and direct-printing process. The modulated characteristics, as exemplified by reconfigurability, ultra-stretchability, and electrical reliability, empower wide fields of researchers to construct functional structures for diverse engineering applications (**Figure 24**).

3.2.1 Kirigami engineering of transparent electrode

In this chapter, by utilizing this simple designing strategy, kirigami engineering has been applied to enable elastic modulation of silver nanowire based flexible transparent electrode into the stretchable transparent electrode.

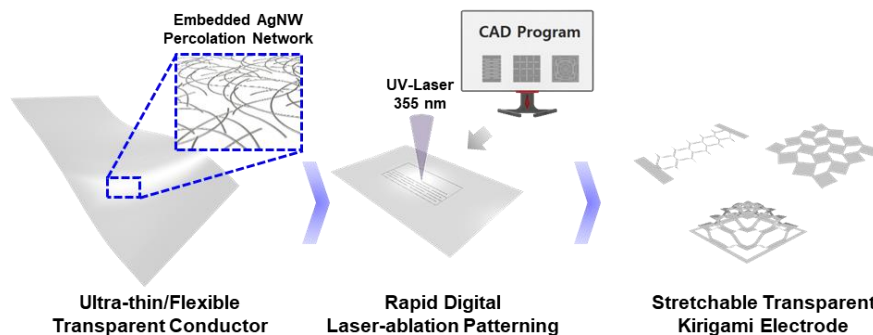


Figure 25 Schematic illustration of digital kirigami cutting process on ultra-thin/flexible NWs/cPI nanocomposite to fabricate various shaped stretchable transparent electrodes.

Transparent electrode composed of AgNWs/cPI already have proven its great flexibility and conductivity in the field of flexible electronics[71, 72]. The beauty of this this approach is that the electrodes can be fabricated rapidly with an aid of laser ablation technique with the desired patterns. By varying the cutting parameter on digital computer-aided design (CAD) program[73], it is able to modulate the strain elongation of transparent conductive nanocomposite materials without generation of patterning masks and fabrication steps in conventional photolithography process.[73] **(Figure 24)** The electrode used in this research generally consists of silver nanowires (AgNWs) and ultra-thin colorless-polyimide (cPI) layer ($<5 \mu\text{m}$) to ensure high optical, thermal, electrical properties and biocompatibility. The novelty of tunable stretchability of kirigami approach can attribute to tailor-designing stretchability range for anywhere on the body since

stretchability required for wearable electronics/E-skins will be different depending on the skin-modulus, body parts, human size and applications.

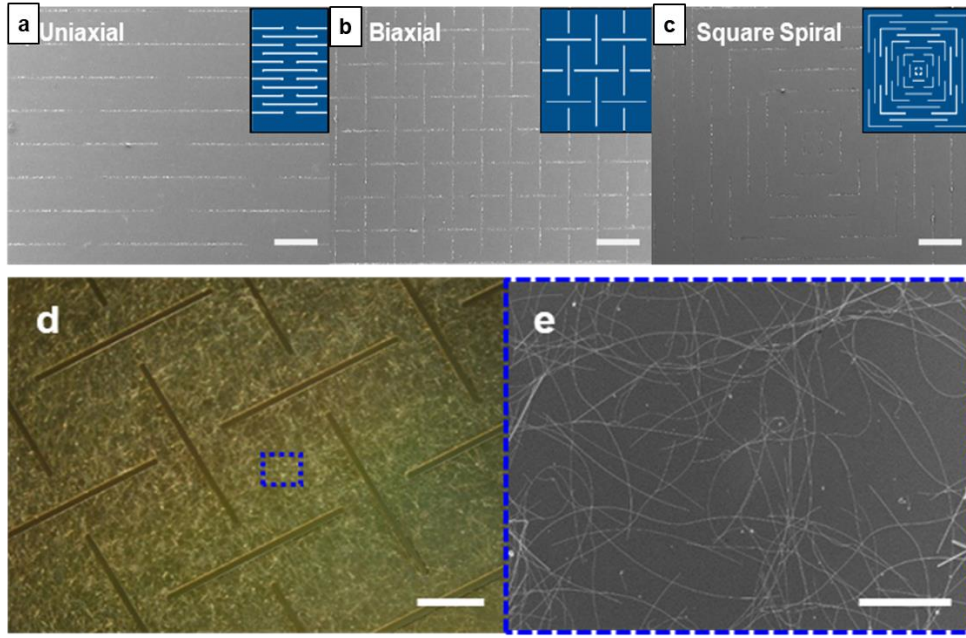


Figure 26 Kirigami patterning of NWs transparent conductor in various shapes. SEM images of various kirigami structures and their 2D designs in the insets: a) Uniaxial, b) Biaxial, and c) Square spiral (Scale bars are 200 μm). d) optical microscope (OM) image of AgNWs/cPI in biaxial kirigami pattern (on the left) and e) SEM images of AgNWs in the magnified blue box (on the right) (Scale bars are 200 μm and 50 μm respectively).

Each kind of kirigami structures earns elasticity on an ultra-thin film, transforms into diverse reconfigurable shapes that attain stretchability, but maintains both high transparency and good conductivity. **Figure 26** shows

SEM images of various 2D cutting geometries on AgNWs/cPI layer in shapes of uniaxial, biaxial and square spiral cuts respectively. Each shapes exhibit stretchable configuration that have unique characteristics for different applications.

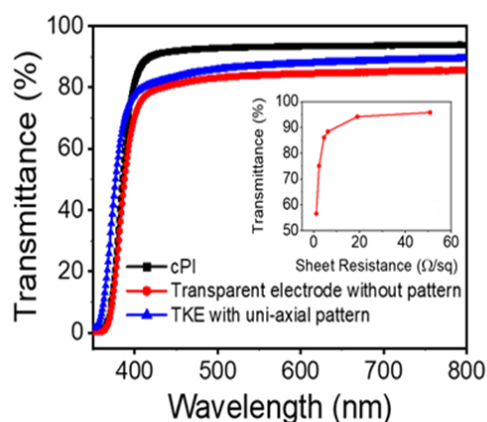


Figure 27 Optical properties of colorless polyimide (cPI), AgNWs/cPI nanocomposite transparent conductor and the transparent conductor with kirigami patterned in uniaxial pattern. Inset graph shows the relationship between electrical and optical properties of the pristine Ag nanowire based transparent electrode.

As shown in **Figure 27**, the ultra-thin AgNWs/cPI conductive layer contains proper amounts of nanomaterials, the UV-Vis spectrum curves of without and with kirigami cuts still exhibit high optical transparency above 80 %, in which they are only visible to micro-nanoscales as seen by optical microscope (OM) and scanning electron microscope (SEM) images in **Figure 26 d-e**.

3.2.2 Force analysis of uni-axial kirigami structure

Although diverse kirigami patterns can be constructed by our laser patterning process, uniaxial pattern is employed to study basic understanding of kirigami structures. Using beam theory, T. Shu et al have derived quations to analyze the force acting on the linear kirigami cut pattern, which may be used for calculating the maximum strain to the failure of the structure.[74]

Here, the deflection, d , and force, F , via the following equation, approximating the beams as two free-end cantilevers joined together:

$$d = \frac{FL^3}{3EI} \text{ (eq. 2)}$$

where L is the beam length, E the Young's modulus of the material, and I the moment of inertia, where

$$I = \frac{wt^3}{12} \text{ (eq. 3)}$$

w is the width of the beam, and t the thickness in the direction of deflection.

Then, it is following

$$d = \frac{4FL^3}{Ewt} \text{ (eq. 4)}$$

Because the two beams are connected in series, the deflection is additive such that

$$d_{beam,total} = d_{beam1} + d_{beam2} = \frac{8FL^3}{Ewt} \text{ (eq. 5)}$$

And then solve for force as a function of deflection, and substituting the

kirigami unit cell parameters,

$$F_{beam} = \frac{Eyt^3}{4\left(\frac{L_c - x}{4}\right)} = \frac{8Edyt^3}{(L_c - x)^3} \quad (\text{eq. 6})$$

The beams in a given row are connected in parallel such that the forces acting on the structure for that row are additive. That is, the force per row, F_{row} , can be expressed as:

$$F_{row} = N_B F_{beam} \quad (\text{eq. 7})$$

where N_B is the total number of beams per row, in the transverse direction.

In the axial direction, the beams from row to row are connected in series, such that the total force acting on the structure, F_{Total} can be expressed as

$$\frac{1}{F_{Total}} = \frac{N_{rows}}{F_{row}} \quad (\text{eq. 8})$$

where N_{rows} is the number of rows along the axial direction. Combining these equations and substituting, the force expression that contains the kirigami unit cell parameters can be:

$$F_{beam} = \frac{8dN_B Eyt^3}{(L_c - x)^3} \quad (\text{eq. 9})$$

The maximum attainable strain (% strain) is the ratio of the final achievable lengths before the structure breaks, ΔL , over the original length, L_0 :

$$\% \text{ strain} = \frac{\Delta L}{L_0} = \frac{(L_c - x)}{2y} \quad (\text{eq. 10})$$

Once the maximum strain is reached, the final yielding varies based on how the cuts grow depending on materials property (in our case, cPI/AgNWs).

3.2.2 Mechanical property of transparent kirigami electrode

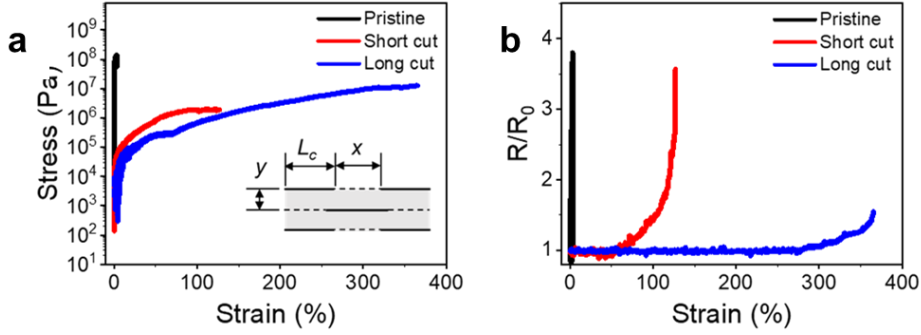


Figure 28 a-b) Stress-strain curves and simultaneously measured resistance changes as a function of strain for TKEs with short (red) and long (blue) cut, and without kirigami cut (black). Unit cell of uniaxial pattern and three key parameters of the unit cell in the inset. Actual cutting lines are marked as black lines.

The equation (eq. 10) suggests that the unit cell parameters control mechanical properties of structures although it does not consider buckling and torsion that actually occur. The unit cell of the uniaxial pattern contains three key parameters: L_c is the cut length, x is the spacing in the horizontal direction and y is the distance in the vertical direction (**Figure 28a**, inset). In this case, the theoretical maximum strain before failure can be attained as equation (1), where ΔL is the incremental length and L_0 is the original length before stretching.[74] To examine the effects of each parameter on the mechanical behavior experimentally, the unit cell parameters L_c , x and y are tested at different value and perform tensile test on the TKEs. First of all,

the mechanical property of a pristine thin film and TKEs with small and large L_c , are compared as shown in **Figure 28a-b**. The pristine AgNWs/cPI composite thin-film breaks out at strain of $\sim 3.2\%$, and the electrical resistance abruptly increases at the same time (**Figure 28a-b**, black curve). Unlike the pristine film, TKEs show significantly different behavior at a wide range of tensile strains. Though the TKEs also show little stress peak at very small strain region ($\sim 5\%$), the kirigami structures gradually dissipates the stress as they go to higher strain region (**Figure 28a, red and blue curves**). Consequently, the electrical resistance of the TKEs remains constant up to specific strain and then begins to increase as it approaches to the strain limitation (**Figure 28b, red and blue curves**).

With handy configurability of the laser patterning process, we could be able to thoroughly study geometrical dependency by easily varying the cutting parameters. The flat and horizontal stable-resistance region, where the resistance does not change, becomes longer as L_c increases and both x and y decrease (**Figure 29d-f**). If the change in kirigami structure does not further induce mechanical deformation of the embedded AgNWs percolation network in the region, there is still on-going out of plane deflection when the TKE is stretched. However, at higher strain above theoretical maximum strain, the cut edges start to tear apart from the due to concentrated stress, resulting in damage to the main body of AgNWs/cPI network that leads to the increase in the resistance.[74-77]

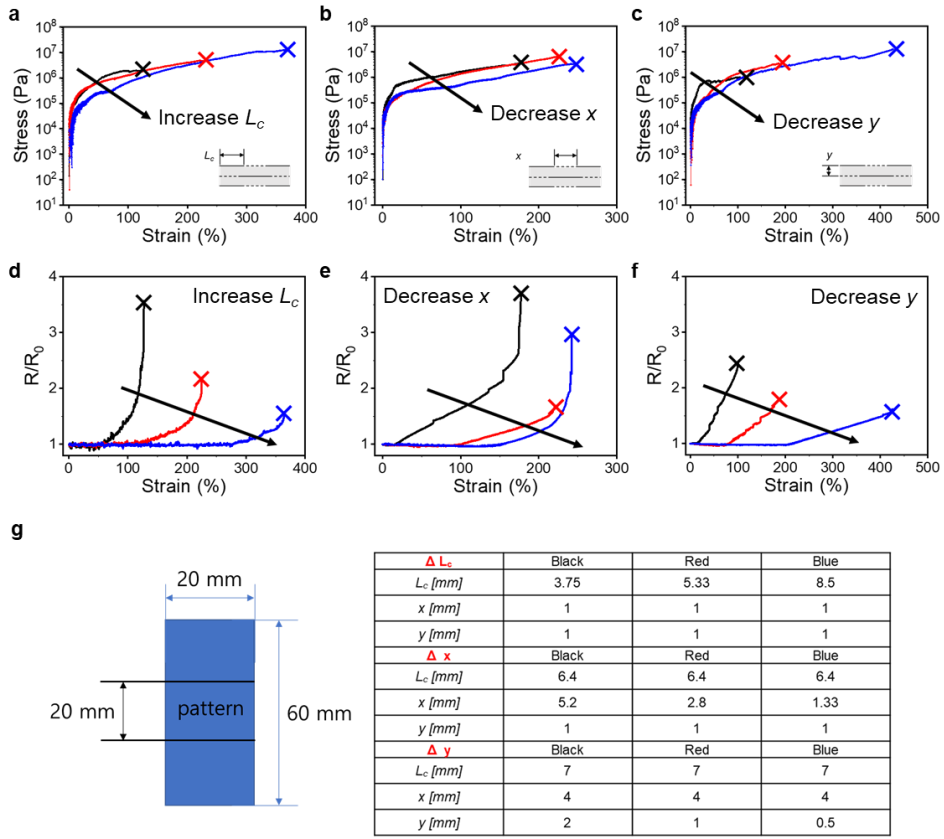


Figure 29 **a-c)** Experimental stress-strain curves of varying kirigami geometries and **d-f)** corresponding electro-mechanical performance with the elongations. **g)** Specified geometries and kirigami parameters of L_c , x and y for investigating mechanical behavior.

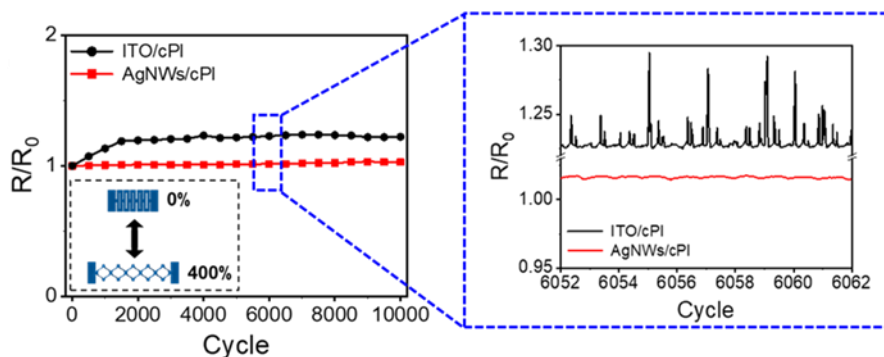


Figure 30 Cyclic bending test of TKE. Resistance changes versus the number of cyclic stretching of ITO/cPI electrode (black) and TKE (red) under the tensile strain of 400%. Magnified regional resistance change under cyclic stretching shown in the dashed blue box.

The other key feature of the TKE is reversibility. As mentioned from the above, TKE have strain-invariant electrical resistance region during one-time stretching; moreover, the resistance lasts constantly under the broad range of strain (0 % to 400 %) and repeated for 10,000 cycles (**Figure 30, red curve**). The shape of TKE returns to the original structure, and the resistance change is negligible within 3% on initial resistance even after 10,000 stretching cycles. Additionally, to verify extreme mechanical reliability of AgNWs/cPI electrode with conventional transparent electrode, cyclic test on kirigami structured indium tin oxide (ITO), which is widely used transparent oxide material, on a cPI layer is also carried out. However, the cyclic stretching of the kirigami patterned ITO/cPI electrode could not endure the bending stress and exhibits the inconsistent and unstable

resistance (**Figure 30, black curve**). The possible reason of the instability is due to brittleness of ITO layer that cracks itself and delaminates between the substrate under mechanical deformation [78-80], leading to the resistance change over 20% at initial cycles (<1500 cycles) and relatively unstable resistance at following cycles (**Figure 30, black curve in blue dotted square**). These electrically invariant and stable while mechanically reversible features of TKE show possibilities of a vast range of electronic skin applications as it can change shapes, modulus and configurability while it is still keeping optical transparency.

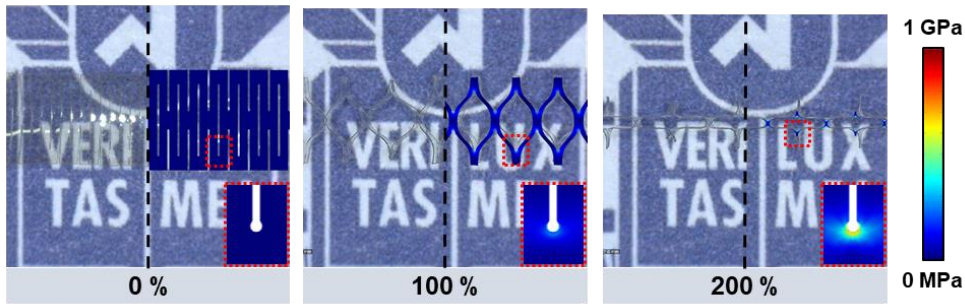


Figure 31 FEM images showing stress distribution of TKE with uniaxial pattern under various tensile strains and corresponding real images. Magnified FEM images of stress-concentrated region under each strain in the insets.

Next, the mechanical behavior is analyzed by observing stress distribution of the TKE under strain by running finite element method (FEM). **Figure 31b** presents out-of-plane buckling deformation of the uniaxial TKE under tensile strain from 0% to 200 % in real and FEM

snapshots. The matched results of experimental and simulation images indicate that the TKE can be elongated to 200 % without a fracture, and the applied stress is well distributed throughout the TKE.

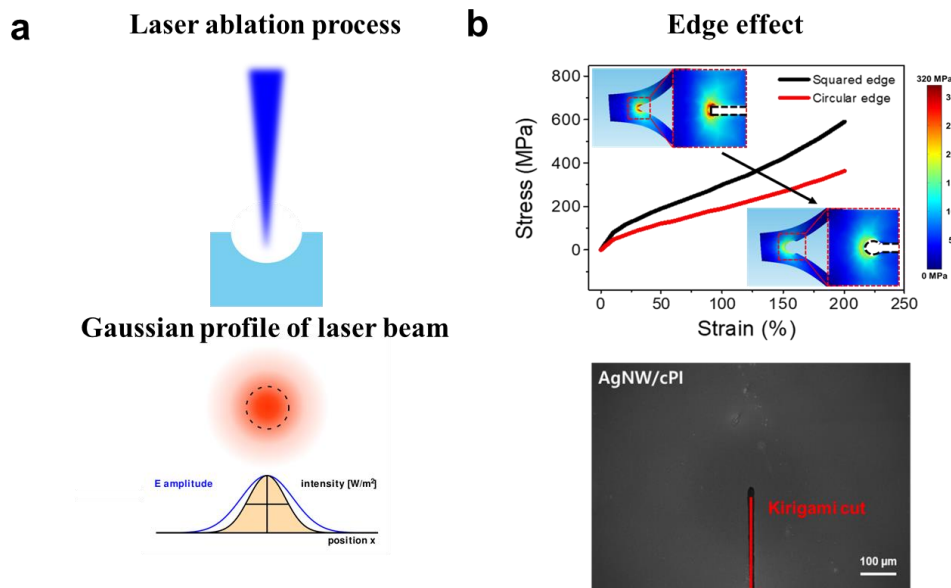


Figure 32 a) illustration of ablation process with Gaussian profile of laser beam. b) Edge effect on mechanical property of kirigami edge using ablation process.

Furthermore, it has been found that there was a circular edge effect that assist stable mechanical property of the kirigami electrode. The cutting edges of the pattern is blunt because the Gaussian energy dispersion of laser beam ablates the electrode along the shape of circular beam spot [73, 81], the laser process assists the distribution of stress effectively without additional setting (**Figure 32**). This circular edge impedes the growth of crack, therefore allowing to withstand higher strain with the circular edge

than the squared edge as shown in their stress-strain curves (**Figure 32**).[74]

3.2.3 Applications of stretchable transparent kirigami electrode

The versatility of this work is demonstrated by ultra-stretchable transparent kirigami heater for personal thermal management and conformal transparent kirigami electrophysiology sensor for continuous health monitoring of human body conditions. Finally, by integrating E-skin sensors with quadrotor drones, it has been successfully demonstrated human-machine-interface using our stretchable transparent kirigami electrodes.

3.2.3.1 Stretchable transparent kirigami heater

As a demonstration of E-skin application, we design and fabricate a transparent kirigami heater (TKH) to suggest the feasibility of personal thermal treatment[56, 82, 83], wearable thermal haptic[84], and wound healing monitoring[85]. **Figure 33** illustrates a schematic structure of the TKH with an enough large area that can cover a wrist of an adult subject.

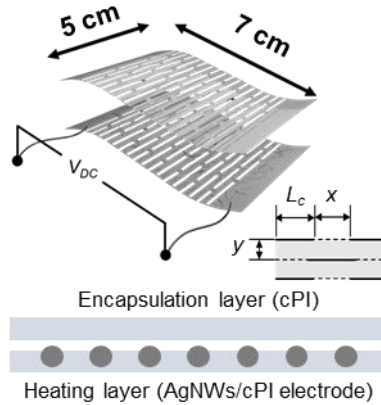


Figure 33 Schematic illustration of uniaxial transparent kirigami heater

(cutting dimensions: $L_c = 15$ mm, $x = 1.7$ mm, and $y = 1.7$ mm).

The TKH consists of two layers: (1) a heating layer consisting of AgNWs/cPI composite and (2) an encapsulation layer composed of cPI layer only (**Figure 33**). Since the AgNWs-exposed side of the TKE should be covered with cPI varnish to prevent current leakage, the whole layers are parallel cut into uniaxial kirigami structure. The thin encapsulated layer prevents current leakage but facilitates the heat flow.

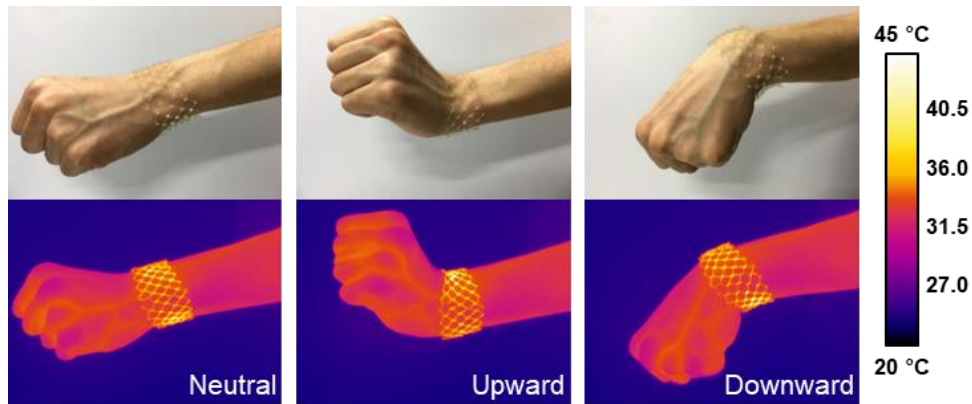


Figure 34 Wearable transparent kirigami heater that operates on the wrist at input voltage of 4.5 V and performs under dynamic movements (upward and downward).

The fabricated transparent kirigami heater (TKH) operates well over a broad range of strains and recovers from dynamic deformations occurring from dynamic movements such as stretching, bending and twisting (As shown in the captured Real/IR images in **Figure 34**).

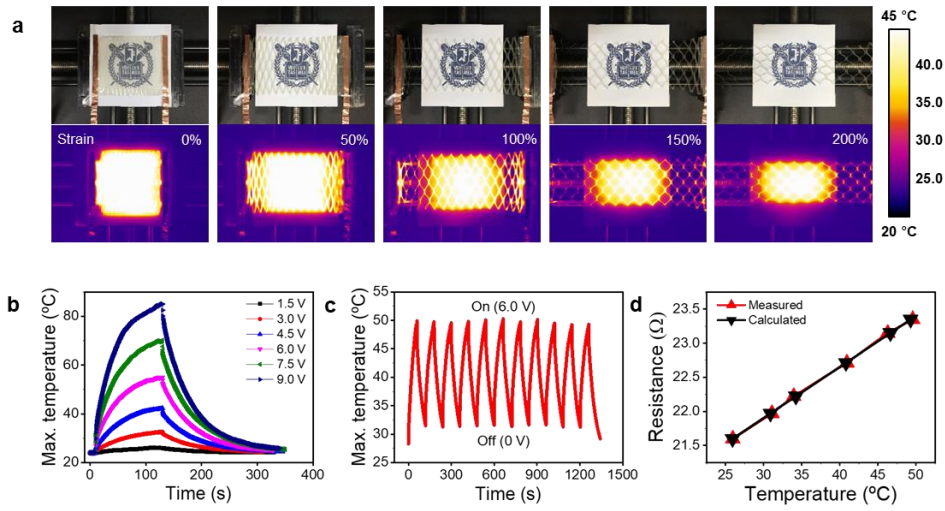


Figure 35 a) Electrothermal and mechanical stability test verified by stretching under strain elongations of 0%, 50%, 100%, 150% and 200%. b) Maximum temperature at increasing input voltages from 1.5V to 9.0V. c) Cyclic operation temperature at 6 V. d) Resistance versus temperature of calculated and measured graph of transparent kirigami heater.

Besides, the TKH shows great structural reversibility and stable electrothermal performances. The TKH can be elongated to a tensile strain of 200%, maintaining constant joule heating temperatures (**Figure 35a**, IR images) and optical transparency (**Figure 35a**, real images). **Figure 35a** also exhibits that the heat dissipated area around contact surface. Because the TKH is designed to stretch out over hundred percentages of strain elongation, it is able to provide thermal treatment over the large area of the skin. The maximum temperature profiles presented in **Figure 35b-c** show time-domain max temperatures by incremental input voltages from 1.5 V to

9.0 V and repetitive voltage of 6.0 V respectively. At an elevated temperature of ~ 80 °C, the TKH operates stably without eletrothermal degradation of the performance, and it gives fast enough thermal response during repetitive voltage on-off cycles. Commonly used conductive materials, especially copper and silver, tend to increase in the resistance respect to the increase in temperature. The TKH is also capable of responding to the change in the electrical resistance of a material depending on temperature since the TKH consists of silver nanowires. The TKH shows the positive linear relationship between the resistance and the temperature. Therefore, the constant dV/dT extracted from the slope of input voltage versus the output temperature graph is used to find out the calculated temperature from the measured resistance as presented in **Figure 35d**. Thus, it rather suggests a distinctive performance of TKE as a wearable temperature sensor measuring human body temperature in real time as well.[85].

3.2.3.2 Stretchable transparent kirigami electrophysiology (EP) sensor

Healthcare monitoring of human body conditions in comfortable and imperceptible way is critically important parts that E-skin devices should take care[43, 86-90]. Commercial electrodes typically used for measuring electrophysiology (EP) signals are not transparent. However, if the electrodes are transparent, transparency can provide a new useful functionality to EP sensors, where the target surface (such as skin) condition

can be directly observable throughout the measurement and this new functionality will be very important especially for EP sensors because the electrode can assist clinical trials to overcome practical hurdles by real-time monitoring while sensing simultaneously.[91] To realize accurate monitoring of bio-potential signals, the strain in such transparent electrode has to be properly modulated in a certain strain region ($<30\%$).

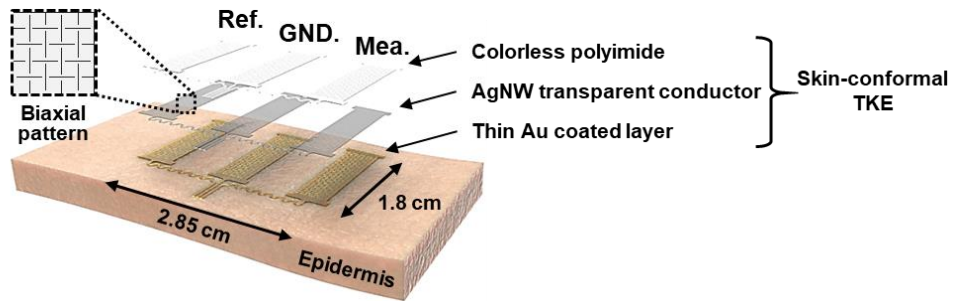


Figure 36 Configuration of transparent kirigami EP sensor for capturing various electrophysiology signals. The TKEs patterned as Ref., GND. and Mea. electrodes with the biaxial pattern and the additional thin Au coated layer at the skin contact.

Figure 36 illustrates the TKE electrophysiology (EP) sensor with a set of three discrete electrodes in the shape of rectangular bars, as reference, ground and measure, is fabricated to acquire high-quality EP signals from nearly any region of the body. Basically, the transparent kirigami electrode composed of AgNWs/cPI and patterned in biaxial kirigami is fabricated, then only AgNWs surface exposed out of cPI layer is selectively replaced with a thin-Au layer (detailed method described in Experimental Section) to

ensure transparency, conformal contact onto the skin and biocompatibility for long-term health monitoring of EP signals.[92] Long-term monitoring of electrophysiology signal using TKEs is enabled because the coating of Au offers oxidation resistive and conductive layer[86] on the exposed surface of silver nanowires to ensure enhanced electrical stability and at the same time improves biocompatibility by preventing allergic reaction of skin from direct contact of silver nanowires.[93]

Moreover, this micro-kirigami pattern adheres along skin morphology with minimal out-of-plane buckling and higher van der Waals adhesive force when the structure tuned to skin-modulus[94, 95], so it validates the advantage of monitoring vital signs using the kirigami-structured transparent electrode. Characteristic of soft and thin but conformal properties of TKE enables to capture various electrophysiology (EP) signals on curvilinear and irregular surfaces of human body (Ex. chest, forehead, temple, forearm, etc.)[86, 89, 96-98]

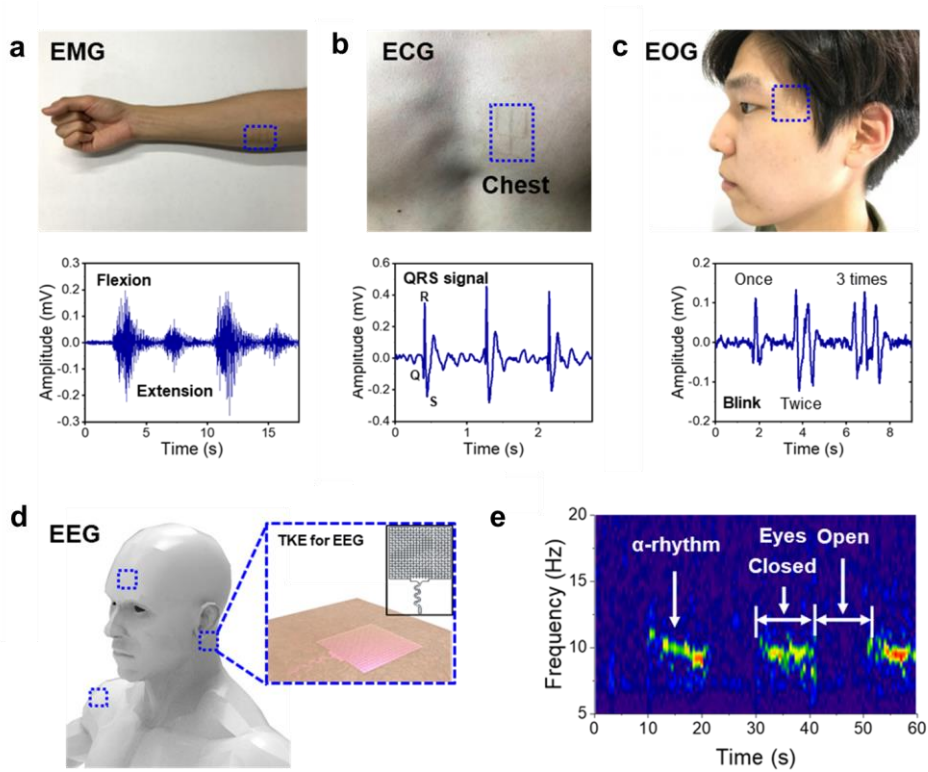


Figure 37 Various electrophysiology signal measurements (locations and signals) for a) EMG, b) ECG and c) EOG. d) Schematic illustration of measurement locations on graphical human model for monitoring EEG signal. e) EEG alpha rhythms observed at 10 Hz.

Figure 37 show the real images of measure locations for monitoring various EP signals such as electromyogram (EMG), electrocardiogram (ECG) and electrooculogram (EOG) at flexor carpi, heart and temple respectively. The surface EMG (sEMG) from forearms is collected using a set of the transparent kirigami EP sensor. Contraction of flexor carpi in flexion is clearly offered large potential difference whereas its extension shows relatively small potential in sEMG signals.

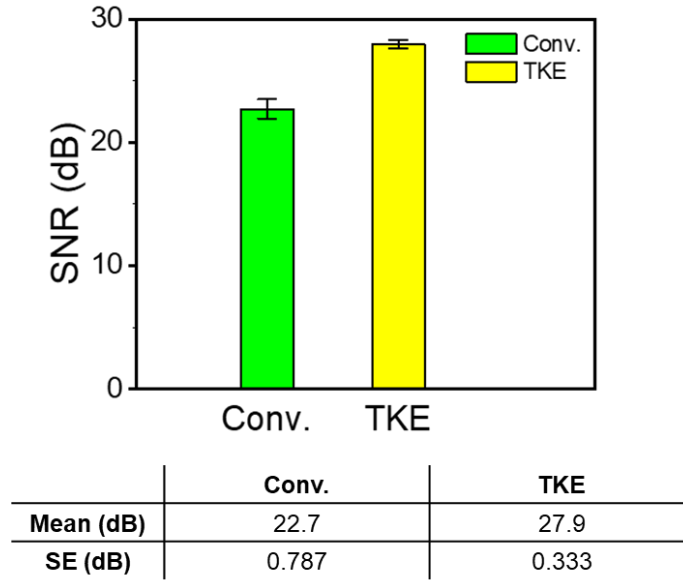


Figure 38 SNR comparison between conventional and TKE EMG signals.

$$\text{Signal to Noise Ratio(SNR)} = \frac{\text{Signal (peak of action potential)}}{\text{Noise (peak of base line noise)}} \quad (\text{eq. 11})$$

The signal to noise ratio (SNR) comparison between conventional electrode and the TKE (**Figure 38**) validates that their sEMG signals are very comparable since the difference in the SNR is only 23 %.

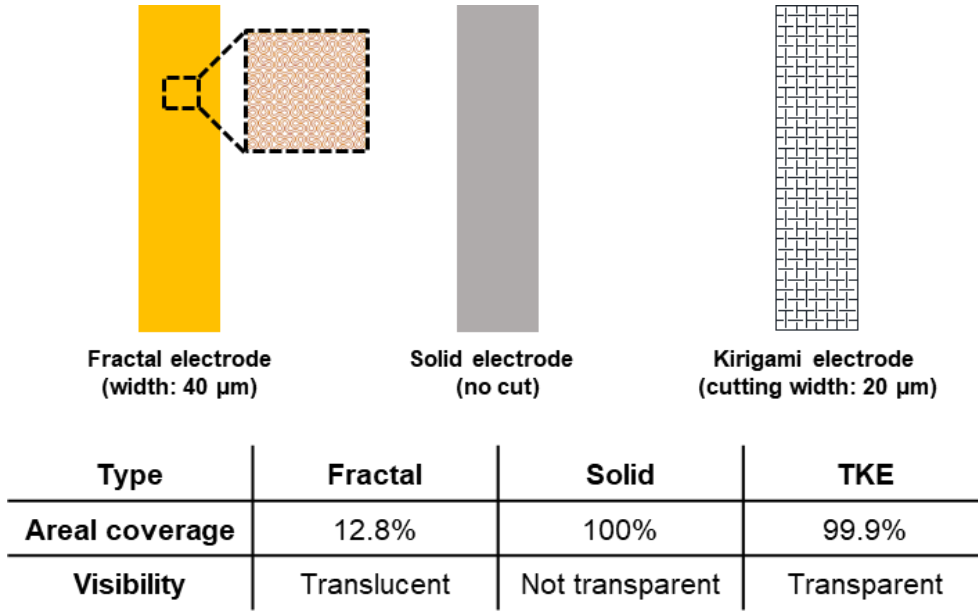


Figure 39 Comparison of areal coverage and visibility between fractal, solid and kirigami electrodes.

Although the TKE maintains optical transparency, this excellent signal quality measured by the TKE may be attributed by its high areal coverage of 99.9 % (**Figure 39**). For measuring ECG signals, the TKE system is placed on a chest near the heart to measure heartbeats in typical form of QRS signal[99]. In order to measure EOG, a miniature set of TKEs is put on the temple near an eye to capture EOG signal from blinking of an eye.[100] The number of blinking is easily classified by observing the number potential differences from EOG signals. Lastly, for monitoring electroencephalography (EEG) signal, a separated set of three TKEs are prepared and placed on forehead, shoulder and the area in between auricle and mastoid that works as reference, ground and measurement electrodes

respectively. **Figure 37a-c** show measured EMG, ECG and EOG for their respective body functions. During forearm extension and flexion, the magnitude of sEMG signal ranges from 0.02 mV to 0.3 mV. Moreover, the amplitudes of the EP signals fall around 0.4 mV, 0.1 mV and 20 μ V in cases of ECG, EOG and EEG, respectively. **Figure 37e** offers EEG spectrum of alpha rhythm in the relaxed state of human body. The spectrogram of EEG is derived by employing short-time Fourier transform with software in MATLAB (R2018b, Mathworks, Natick, MA). At near 8~12 Hz frequency, alpha rhythm clearly appears in relaxed state of human body (classified by opening/closing of eyes)[101]

Adhesion of transparent kirigami electrode

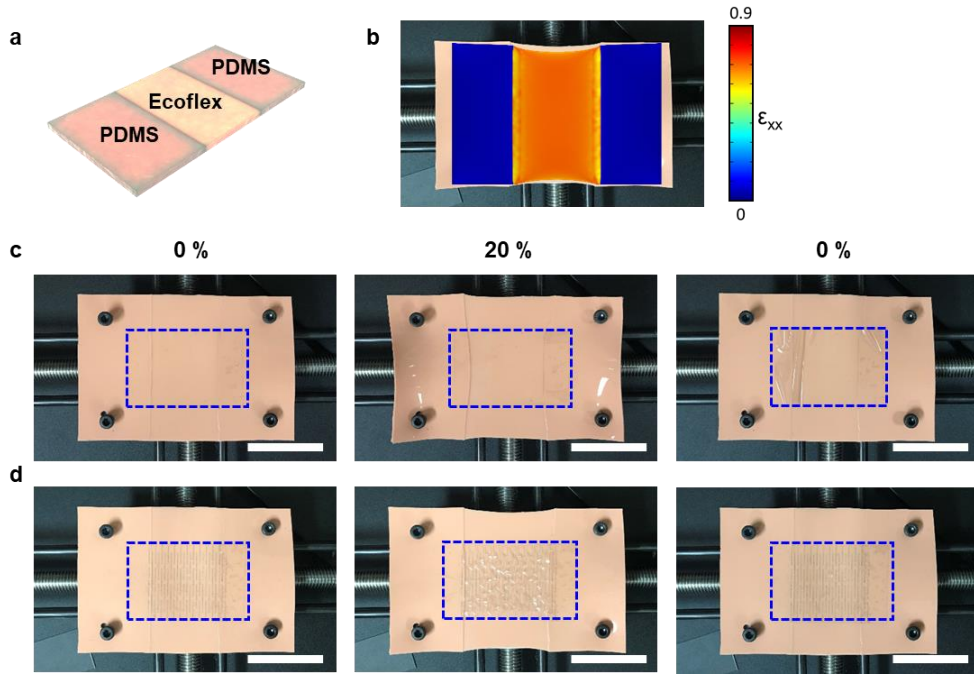


Figure 40 a) Schematic illustration of skin-colored inhomogeneous

elastomeric substrate for adhesion test. b) Stress distribution result of inhomogeneous elastomer when strain of 20% is applied. Adhesion test for c) pristine thin film versus d) kirigami thin film (scale bars are 3.5 cm).

Adhesion of kirigami patterned thin-film compared to pristine film is also extensively related to conformal contact onto the skin.[94] As depicted **Figure 40**, the comparison of stretching configuration at 20 % strain with pristine and the kirigami thin-films on inhomogeneous elastomeric substrates demonstrate that the kirigami thin-film exhibits much better mechanical reversibility without delamination phenomena from the skin replica. These trends of mechanical and electrical properties are tunable depending on the unit cell parameters.

Long-term/biocompatible monitoring

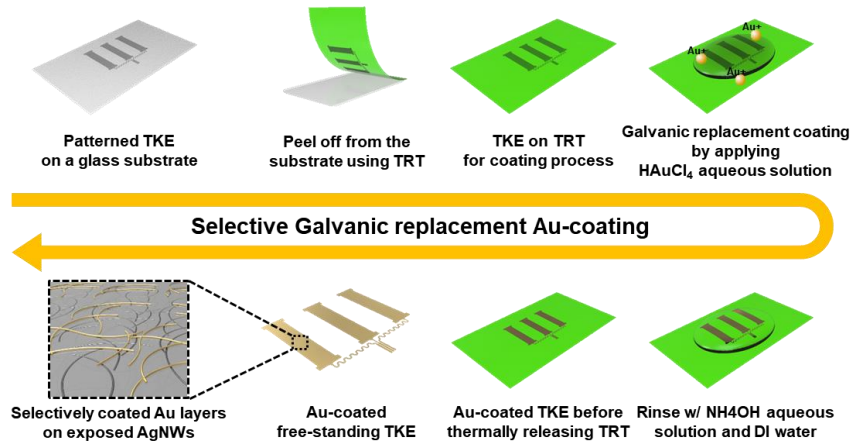


Figure 41 Schematics of selective galvanic replacement gold (Au) coating process.

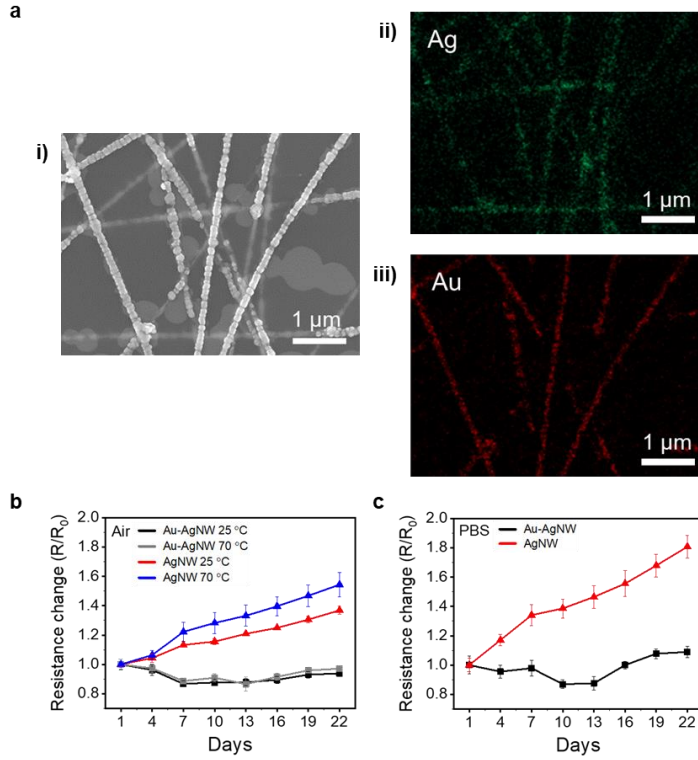


Figure 42 a) EDS image that shows Au layers coated selectively on the exposed surface of the AgNWs. i) SEM image, ii) Ag only, and iii) Au only. b) Oxidization stability test in thermally accelerated condition. c) Biocompatibility test via immersion in phosphate buffered solution (PBS) solution.

Long-term monitoring of EP signals using the electrode is realized by coating non-toxic, oxidization resistant material, in this case gold (Au), on the exposed surface of AgNWs.[43] Enhanced electrical stability under environmental/sweating condition after galvanic coating process of Au [102] also assists stable long-term monitoring of the electronics (**Figure 42**).[101] Because the coating of Au offers oxidization resistive and

conductive layer[9]on top of the exposed surface of silver nanowires to ensure enhanced electrical stability and at the same time improves biocompatibility by preventing allergic reaction of skin from direct contact of silver nanowires.[93]

3.2.3.3 Human-machine interface using TKE

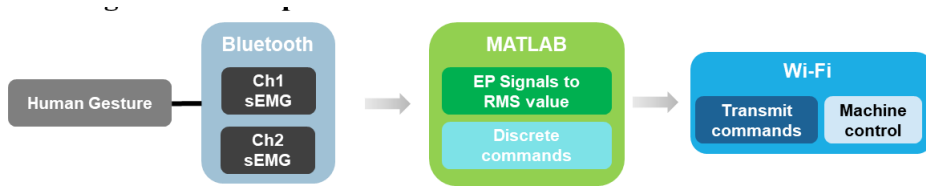


Figure 43 Flow diagram of human-machine interface using TKE.

Human-machine interface (HMI) demonstration using the transparent kirigami electrode is crucial to exhibit because it refers that human body and computer/machine are closely linked by E-skin sensor (**Figure 43**).

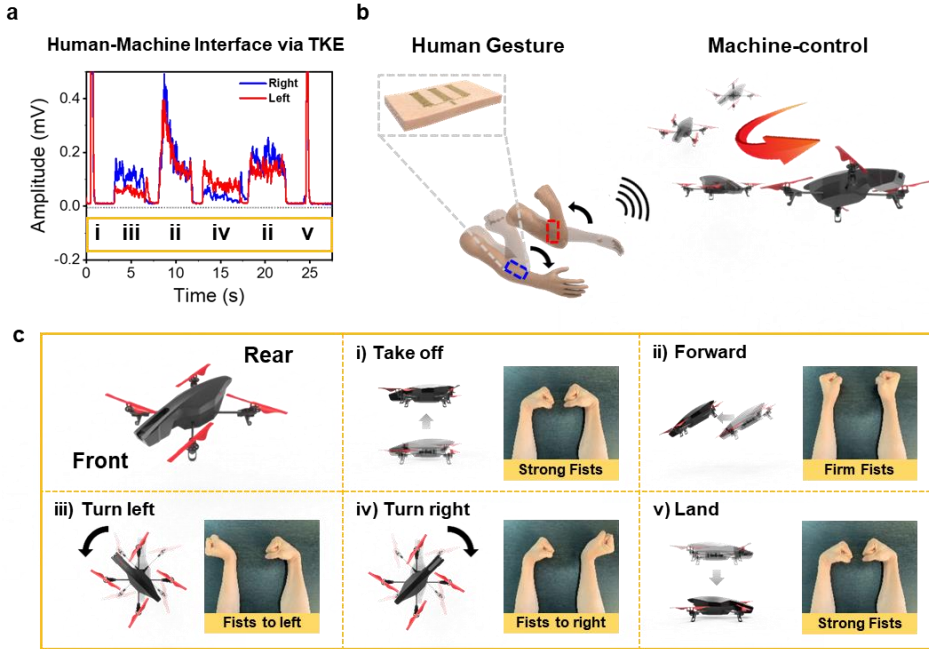


Figure 44 Human-machine interface using transparent kirigami electrodes.

a) Two sets of measured sEMG signals from both forearms using TKE sensors. Roman numerals enclosed in the orange box under the RMS signals represent corresponding commands in c). b) Schematic illustration of demonstrating human-machine interface via TKEs by controlling a quadrotor with the gestures, which are signal processed by Bluetooth and WiFi-network. c) Description of control motions and corresponding gestures: i) Take off, ii) Fly forward, iii) Turn left, iv) Turn right, and v) Land.

Figure 44a depicts two sets of sEMG signals measured from both left/right forearms for controlling a quadrotor drone with using specific gestures and wifi-network connection as graphically explained in **Figure**

44b-c. Figure 44c illustrates a quadrotor drone motions respect to command classification using EMG signals for HMI. Generation of sEMG from potential difference of flexor carpi in motions of flexion and extension are utilized to control a quadcopter drone (AR. Drone, Parrot SA, Paris). Our bimanual gestures for commands include: (1) strong fists, (2) firm fists (3) fists to the left and (4) fists to the right. From the raw data produced by these motions, their root-mean-square (RMS) values are transferred using the equation (2), where n is the number of samples and x_k means the k^{th} sample.

$$RMS = \sqrt{\frac{1}{n} \sum_{k=1}^n x_k^2} \quad (\text{eq. 12})$$

According to custom classification algorithm in MATLAB, the bimanual motions are paired with different five commands—Strong fists: ‘take off and land’, firm fists: ‘fly forward’, fists to the left: ‘turn left’, and fists to the right: ‘turn right’. Before set to flight, we firstly analyze our sEMG signals on both channels of right and left forearms then establish discrete regions with boundary values for classifying commands with RMS values.



Figure 45 (Left) Description of control motions and corresponding gestures: i) Take off, ii) Fly forward, iii) Turn left, iv) Turn right, and v) Land. (Right) The route of a quadrotor drone in HMI demonstration and its corresponding real images arranged as numbers in order.

The route for demonstration of controlling a quadrotor drone is drawn in **Figure 45**. The flight manipulation of a quadrotor drone along the route is successfully demonstrated as shown in real images with numbers in the order.

3.2.3.4 Experimental section for stretchable transparent kirigami electrode

Fabrication of transparent kirigami electrodes: On a glass substrate, AgNWs are deposited using vacuum filtration process, and cPI varnish (Kolon) in DMSO is spin-coated over the area. By utilizing pulsed laser ablation process, both AgNWs and cPI layers are patterned rapidly at the same time in desired-shaped kirigami structure. Finally, the patterned AgNWs/cPI nanocomposite with kirigami structure is easily peeled from the substrate.

Fabrication of AgNWs/cPI electrode: Depending on the desired transparency and electrical NWs transparent conductor, proper amounts of AgNWs dispersed in ethanol are transferred on a glass substrate by vacuum filtration method. Usually, 300 μ L of AgNWs dispersed in EtOH (0.015 wt %) is used for the deposition of AgNWs throughout experiments. The transferred AgNWs are thermally annealed on a hotplate at 200 °C for 30 min. onto the annealed AgNWs, cPI varnish is spin-coated at 700 rpm for 60 seconds and baked sequentially at 150°C for 5 min and 260 °C for 30 min. The kirigami patterned AgNWs/cPI composite electrode is carefully peeled off from the glass with a water soluble tape (Aquasol) attached on the top and dissolved. Thus, the resultant electrode is composed of the AgNWs that are embedded in the cPI thin film with partially exposed part of the AgNWs.

Laser ablation patterning process: The AgNWs/cPI electrode on the glass substrate is irradiated with a Q-switched DPSS laser to ablate the electrode along kirigami pattern. The laser operates at the wavelength of 355 nm, the pulse repetition rate of 30 kHz and the pulse width with 35 nanoseconds. The beam spot successfully follows desired kirigami pattern by using a 2-axis Galvano mirror scanner. The focused beam spot width is approximately 20 μ m so the ablated spot diameter falls under 20 μ m. The control parameters repetitions, current power %, and scanning speed are carefully adjusted to ablate the desired patterns.

Gold coating on the exposed AgNWs: Gold layer is coated on the exposed

AgNWs of TKE by the galvanic replacement process modified from previous study.[102, 103] The first step of gold coating by the galvanic replacement process involves placing as-patterned TKE in gold(III) chloride trihydrate solution ($\text{HAuCl}_4 \cdot 3\text{H}_2\text{O}$ (Sigma Aldrich), 0.3 mM dilution with deionized water) for 10 min. Followed by the replacement process, the TKE is dipped in 28 % of aqueous solution of ammonia (NH_4OH , Sigma Aldrich) for 1 min to remove silver chloride (AgCl) produced around the Au-AgNWs.

Finite element simulation: FEM analysis provides the mechanical deformation behavior and the stress distribution of the stretched structures with various kirigami pattern designs. Free triangular element is chosen as a mesh of which size ranges from 0.01 mm to 0.15 mm. We use two techniques to avoid bifurcation of the buckling: 1) one is related to a boundary condition and 2) another one is in a study method. We set a prescribed displacement boundary condition at both ends of the structures. The boundary condition consists of not only displacement in the axial direction but also displacement perturbation in the plane-normal direction. Because the size of the perturbation is close to 0.1 % of the minimum element size, it does not have significant effect on the stress-strain relationship. Furthermore, we apply an auxiliary sweep method so that the simulating calculation runs with the incrementally increasing displacement value. These techniques help the buckling occurs in the one direction.

Measurement of EP signals: All measurements of the EP signals are collected by using the BioRadio wireless physiology monitor (Great Lakes NeuroTechnologies, Independence, OH). The sampling rate is 1 kHz and gain is 1,000 for amplifying the EP signals.

3.3 Conclusion

In summary, a novel concept of transparent and stretchable kirigami electrodes consisting of ultra-thin and flexible AgNWs/cPI composites with laser-patterned kirigami structure, where thin-Au is preferentially coated layer at last depending on applications, has been proposed. The laser patterning technique provides digital and rapid process without requirement of patterning masks and fabrication steps in conventional photolithography process. By utilizing the laser patterning process, a configurable design of kirigami structures enable the transparent electrodes with tunable stretchability, which have strain limit from nearly zero strain to large strain over 400 %, that extends the scope of applications. Biocompatibility and enhanced electrical stability against oxidation are simultaneously attained by Au coating on the exposed surface of AgNWs while having long-term monitoring for various EP signals without skin irritations. Furthermore, owing to soft and ultra-thin but highly stretchable characteristic, our TKE conformally covers the curvilinear and irregular surfaces of human body, facilitating measurement of sEMG on both forearms with dynamic motions in real time for controlling a drone in an advanced form for the

demonstration of HMI. Based on these notable properties of TKE, this proposed concepts and approach will open up various possibilities of providing multi-functional transparent and wearable electronic skin applications.

Chapter 4. Summary and Future Work

In this work, I have proposed synthesis, fabrication and structural design approach to engineer silver nanowires (AgNWs) based transparent electrode thereby improving mechanical, electrical and optical properties in a lightweight, flexible and even stretchable form. Despite the fact that widely used transparent conducting material, indium tin oxide (ITO), has been dominated transparent conductor industry for applications in display, touch panel and solar cells, as the most competitive candidate of among its alternatives, high performance Ag nanowire based transparent conductor has been demonstrated both in physical properties and device performances through engineering the structure or utilizing phenomenon at nano-micro scales. In this work, the engineering approaches to enhance the performance of silver nanowires based flexible transparent flexible conductor involved the combination nanowires at two different nano-micro-scales to synergistically back-up one another by their roles in transparent conductive network and employment of swelling phenomenon of a polyurethane layer as a mechanically welding / embedding layer in room temperature scalable fabrication of silver nanowire based transparent conductor. Furthermore,

kirigami technique to engineer designs at micro-scales enables a transformative impact on silver nanowire based flexible transparent electrode into stretchable transparent electrode allowing it to be used as ultra-stretchable or skin-conformal electronics that could be demonstrated as wearable health-monitoring devices and sensors that connect human gestures and a drone manipulation for human-machine interaction.

Future work of this research will continue with different synthesis mechanism that produces meaning dimensions of the nanowire, fabrication approach that improves instability, scalability and performances and various other applications that utilizes transparency and conductivity. As it always have been, nanowires based electronics will further attribute the field of flexible / stretchable electronics.

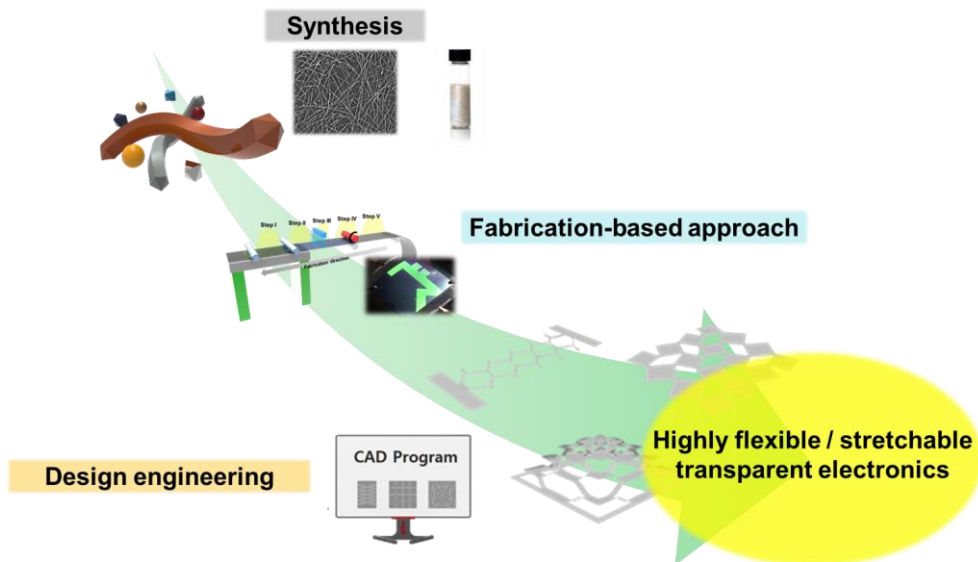


Figure 46 Engineering structure of silver nanowires based transparent electrode for highly flexible / stretchable transparent electronics.

Bibliography

1. Hu, M., et al., *Flexible transparent PES/silver nanowires/PET sandwich-structured film for high-efficiency electromagnetic interference shielding*. Langmuir, 2012. **28**(18): p. 7101–7106.
2. Abbasi, N.M., et al., *Preparation of silver nanowires and their application in conducting polymer nanocomposites*. Materials Chemistry and Physics, 2015. **166**: p. 1–15.
3. Yang, C., et al., *Silver nanowires: from scalable synthesis to recyclable foldable electronics*. Advanced materials, 2011. **23**(27): p. 3052–3056.
4. Zhou, Y., et al., *Multifunctional TiO₂-Coated Ag Nanowire Arrays as Recyclable SERS Substrates for the Detection of Organic Pollutants*. European Journal of Inorganic Chemistry, 2012. **2012**(19): p. 3176–3182.
5. Kumar, A. and C. Zhou, *The race to replace tin-doped indium oxide: which material will win?* ACS nano, 2010. **4**(1): p. 11–14.
6. Hecht, D.S., L. Hu, and G. Irvin, *Emerging transparent electrodes based on thin films of carbon nanotubes, graphene, and metallic nanostructures*. Advanced materials, 2011. **23**(13): p. 1482–1513.
7. Ellmer, K., *Past achievements and future challenges in the development of optically transparent electrodes*. Nature Photonics, 2012. **6**(12): p. 809–817.
8. Song, C.-H., et al., *Intense-pulsed-light irradiation of Ag nanowire-based transparent electrodes for use in flexible organic light emitting diodes*. Organic Electronics, 2015. **17**: p. 208–215.
9. Liu, Y.-S., et al., *Highly flexible organic-inorganic hybrid perovskite light-emitting devices based on an ultrathin Au electrode*. Optics Letters, 2018. **43**(22): p. 5524–5527.
10. Zhang, M., et al., *All-solution processed transparent organic light emitting diodes*. Nanoscale, 2015. **7**(47): p. 20009–20014.
11. Jung, E.D., et al., *Highly efficient flexible optoelectronic devices using metal nanowire-conducting polymer composite transparent electrode*. Electronic Materials Letters, 2015. **11**(5): p. 906–914.
12. Chang, J.-H., et al., *A solution-processed molybdenum oxide treated silver nanowire network: a highly conductive transparent conducting electrode with superior mechanical and hole injection properties*. Nanoscale, 2015. **7**(10): p. 4572–4579.
13. Lee, H., et al., *Highly efficient and low voltage silver nanowire-based OLEDs employing a n-type hole injection layer*. Nanoscale, 2014. **6**(15): p. 8565–8570.
14. Bari, B., et al., *Simple hydrothermal synthesis of very-long and thin silver nanowires and their application in high quality transparent*

- electrodes*. Journal of Materials Chemistry A, 2016. **4**(29): p. 11365–11371.
15. Bergin, S.M., et al., *The effect of nanowire length and diameter on the properties of transparent, conducting nanowire films*. Nanoscale, 2012. **4**(6): p. 1996–2004.
 16. Lopez-Diaz, D., C. Merino, and M. Velázquez, *Modulating the optoelectronic properties of silver nanowires films: Effect of capping agent and deposition technique*. Materials, 2015. **8**(11): p. 7622–7633.
 17. Kim, S., et al., *Highly reliable AgNW/PEDOT: PSS hybrid films: efficient methods for enhancing transparency and lowering resistance and haziness*. Journal of Materials Chemistry C, 2014. **2**(28): p. 5636–5643.
 18. Sorel, S., et al., *The dependence of the optoelectrical properties of silver nanowire networks on nanowire length and diameter*. Nanotechnology, 2012. **23**(18): p. 185201.
 19. Araki, T., et al., *Low haze transparent electrodes and highly conducting air dried films with ultra-long silver nanowires synthesized by one-step polyol method*. Nano Research, 2014. **7**(2): p. 236–245.
 20. Jiu, J., et al., *Facile synthesis of very-long silver nanowires for transparent electrodes*. Journal of Materials Chemistry A, 2014. **2**(18): p. 6326–6330.
 21. He, X., et al., *A highly conductive, flexible, transparent composite electrode based on the lamination of silver nanowires and polyvinyl alcohol*. Journal of Materials Chemistry C, 2014. **2**(45): p. 9737–9745.
 22. Nam, S., et al., *Ultrasmooth, extremely deformable and shape recoverable Ag nanowire embedded transparent electrode*. Scientific reports, 2014. **4**(1): p. 1–7.
 23. Giebink, N.C. and S. Forrest, *Quantum efficiency roll-off at high brightness in fluorescent and phosphorescent organic light emitting diodes*. Physical Review B, 2008. **77**(23): p. 235215.
 24. Lee, H., et al., *Highly efficient and low voltage silver nanowire-based OLEDs employing a n-type hole injection layer*. 2014. **6**(15): p. 8565–8570.
 25. Song, C.-H., et al., *Intense-pulsed-light irradiation of Ag nanowire-based transparent electrodes for use in flexible organic light emitting diodes*. 2015. **17**: p. 208–215.
 26. Liu, Y.-s., et al., *Ultrasmooth, highly conductive and transparent PEDOT: PSS/silver nanowire composite electrode for flexible organic light-emitting devices*. 2016. **31**: p. 247–252.
 27. Ok, K.-H., et al., *Ultra-thin and smooth transparent electrode for flexible and leakage-free organic light-emitting diodes*. 2015. **5**(1): p. 1–8.
 28. Zhang, M., et al., *All-solution processed transparent organic light emitting diodes*. 2015. **7**(47): p. 20009–20014.
 29. Zeng, X.Y., et al., *A new transparent conductor: silver nanowire film*

- buried at the surface of a transparent polymer*. 2010. **22**(40): p. 4484–4488.
30. Kang, S., et al., *Capillary printing of highly aligned silver nanowire transparent electrodes for high-performance optoelectronic devices*. 2015. **15**(12): p. 7933–7942.
31. Jung, E.D., et al., *Highly efficient flexible optoelectronic devices using metal nanowire-conducting polymer composite transparent electrode*. 2015. **11**(5): p. 906–914.
32. Yu, Z., et al., *Highly flexible silver nanowire electrodes for shape-memory polymer light-emitting diodes*. 2011. **23**(5): p. 664–668.
33. Chang, J.-H., et al., *A solution-processed molybdenum oxide treated silver nanowire network: a highly conductive transparent conducting electrode with superior mechanical and hole injection properties*. 2015. **7**(10): p. 4572–4579.
34. Park, J.H., et al., *Flash-induced self-limited plasmonic welding of silver nanowire network for transparent flexible energy harvester*. *Advanced Materials*, 2017. **29**(5): p. 1603473.
35. Lee, J., et al., *Room-temperature nanosoldering of a very long metal nanowire network by conducting-polymer-assisted joining for a flexible touch-panel application*. *Advanced Functional Materials*, 2013. **23**(34): p. 4171–4176.
36. Jeong, H., et al., *Fabrication of Transparent Conductive Film with Flexible Silver Nanowires Using Roll-to-Roll Slot-Die Coating and Calendering and Its Application to Resistive Touch Panel*. *Advanced Electronic Materials*, 2018. **4**(11): p. 1800243.
37. Cui, Z., F.R. Pobleto, and Y. Zhu, *Tailoring the temperature coefficient of resistance of silver nanowire nanocomposites and their application as stretchable temperature sensors*. *ACS applied materials & interfaces*, 2019. **11**(19): p. 17836–17842.
38. Ding, Y., et al., *Welded silver nanowire networks as high-performance transparent conductive electrodes: Welding techniques and device applications*. *Applied Materials Today*, 2020. **20**: p. 100634.
39. Won, P., et al., *Transparent Soft Actuators/Sensors and Camouflage Skins for Imperceptible Soft Robotics*. *Advanced Materials*, 2020: p. 2002397.
40. Yamada, T., et al., *A stretchable carbon nanotube strain sensor for human-motion detection*. *Nature nanotechnology*, 2011. **6**(5): p. 296.
41. Jeong, J.W., et al., *Materials and optimized designs for human-machine interfaces via epidermal electronics*. *Advanced Materials*, 2013. **25**(47): p. 6839–6846.
42. Yan, C., et al., *Highly stretchable piezoresistive graphene-nanocellulose nanopaper for strain sensors*. *Advanced materials*, 2014. **26**(13): p. 2022–2027.
43. Miyamoto, A., et al., *Inflammation-free, gas-permeable, lightweight, stretchable on-skin electronics with nanomeshes*. *Nature*

- nanotechnology, 2017. **12**(9): p. 907.
44. Gong, S., et al., *A wearable and highly sensitive pressure sensor with ultrathin gold nanowires*. Nature communications, 2014. **5**(1): p. 1–8.
 45. Zhang, Y., et al., *A mechanically driven form of Kirigami as a route to 3D mesostructures in micro/nanomembranes*. Proceedings of the National Academy of Sciences, 2015. **112**(38): p. 11757–11764.
 46. Yeo, W.H., et al., *Multifunctional epidermal electronics printed directly onto the skin*. Adv. Mater., 2013. **25**(20): p. 2773–8.
 47. Kim, D.H., et al., *Epidermal electronics*. Science, 2011. **333**(6044): p. 838–43.
 48. Lee, C.H., et al., *Soft core/shell packages for stretchable electronics*. Adv. Funct. Mater., 2015. **25**(24): p. 3698–3704.
 49. Kaltenbrunner, M., et al., *An ultra-lightweight design for imperceptible plastic electronics*. Nature, 2013. **499**(7459): p. 458–63.
 50. Drack, M., et al., *An imperceptible plastic electronic wrap*. Adv. Mater., 2015. **27**(1): p. 34–40.
 51. Amjadi, M., et al., *Stretchable, skin-mountable, and wearable strain sensors and their potential applications: a review*. Adv. Funct. Mater., 2016. **26**(11): p. 1678–1698.
 52. Jang, K.I., et al., *Soft network composite materials with deterministic and bio-inspired designs*. Nat. Commun., 2015. **6**: p. 6566.
 53. Someya, T., S. Bauer, and M. Kaltenbrunner, *Imperceptible organic electronics*. MRS Bull., 2017. **42**(2): p. 124–130.
 54. Brosteaux, D., et al., *Design and fabrication of elastic interconnections for stretchable electronic circuits*. IEEE Electron Device Lett., 2007. **28**(7): p. 552–554.
 55. Hsu, P.C., et al., *Personal thermal management by metallic nanowire-coated textile*. Nano Lett., 2015. **15**(1): p. 365–71.
 56. Choi, S., et al., *Stretchable heater using ligand-exchanged silver nanowire nanocomposite for wearable articular thermotherapy*. ACS nano, 2015. **9**(6): p. 6626–6633.
 57. Lee, H.B., et al., *Mogul-Patterned Elastomeric Substrate for Stretchable Electronics*. Adv. Mater., 2016. **28**(16): p. 3069–77.
 58. Fan, J.A., et al., *Fractal design concepts for stretchable electronics*. Nat. Commun., 2014. **5**: p. 3266.
 59. Norton, J.J., et al., *Soft, curved electrode systems capable of integration on the auricle as a persistent brain-computer interface*. Proc. Natl. Acad. Sci. U. S. A., 2015: p. 201424875.
 60. Guo, H., et al., *All-in-One Shape-Adaptive Self-Charging Power Package for Wearable Electronics*. ACS Nano, 2016. **10**(11): p. 10580–10588.
 61. Wu, C., et al., *Paper based triboelectric nanogenerators made of stretchable interlocking kirigami patterns*. ACS Nano, 2016. **10**(4): p. 4652–4659.
 62. Yokota, T., et al., *Ultraflexible organic photonic skin*. Sci. Adv., 2016.

- 2(4): p. e1501856.
63. Jang, N.S., et al., *Simple Approach to High-Performance Stretchable Heaters Based on Kirigami Patterning of Conductive Paper for Wearable Thermotherapy Applications*. ACS Appl. Mater. Interfaces, 2017. **9**(23): p. 19612–19621.
 64. Lv, Z., et al., *Editable Supercapacitors with Customizable Stretchability Based on Mechanically Strengthened Ultralong MnO₂ Nanowire Composite*. Adv. Mater., 2018. **30**(2): p. 1704531.
 65. Hattori, Y., et al., *Multifunctional skin-like electronics for quantitative, clinical monitoring of cutaneous wound healing*. Adv. Healthcare Mater., 2014. **3**(10): p. 1597–607.
 66. Sekitani, T., et al., *A rubberlike stretchable active matrix using elastic conductors*. Science, 2008. **321**(5895): p. 1468–1472.
 67. Zhang, Y., et al., *Polymer-embedded carbon nanotube ribbons for stretchable conductors*. Adv. Mater., 2010. **22**(28): p. 3027–31.
 68. Kim, Y., et al., *Stretchable nanoparticle conductors with self-organized conductive pathways*. Nature, 2013. **500**(7460): p. 59–63.
 69. Ho, M.D., et al., *Percolating network of ultrathin gold nanowires and silver nanowires toward “invisible” wearable sensors for detecting emotional expression and apexcardiogram*. Adv. Funct. Mater., 2017. **27**(25): p. 1700845.
 70. Ho, M.D., et al., *Fractal Gold Nanoframework for Highly Stretchable Transparent Strain-Insensitive Conductors*. Nano Lett., 2018. **18**(6): p. 3593–3599.
 71. Kim, Y., et al., *Inverted layer-by-layer fabrication of an ultraflexible and transparent Ag nanowire/conductive polymer composite electrode for use in high-performance organic solar cells*. Adv. Funct. Mater., 2015. **25**(29): p. 4580–4589.
 72. Pyo, K.-h. and J.-W. Kim, *Thermally stable and flexible transparent heaters based on silver nanowire-colorless polyimide composite electrode*. Curr. Appl. Phys., 2016. **16**(11): p. 1453–1458.
 73. Hong, S., et al., *Selective laser direct patterning of silver nanowire percolation network transparent conductor for capacitive touch panel*. Journal of nanoscience and nanotechnology, 2015. **15**(3): p. 2317–2323.
 74. Shyu, T.C., et al., *A kirigami approach to engineering elasticity in nanocomposites through patterned defects*. Nature materials, 2015. **14**(8): p. 785–789.
 75. Xu, R., et al., *Kirigami-inspired, highly stretchable micro-supercapacitor patches fabricated by laser conversion and cutting*. Microsystems & Nanoengineering, 2018. **4**(1): p. 36.
 76. Lv, Z., et al., *Editable supercapacitors with customizable stretchability based on mechanically strengthened ultralong MnO₂ nanowire composite*. Advanced Materials, 2018. **30**(2): p. 1704531.
 77. Jang, N.-S., et al., *Simple approach to high-performance stretchable heaters based on kirigami patterning of conductive paper for wearable thermotherapy applications*. ACS applied materials &

- interfaces, 2017. **9**(23): p. 19612–19621.
78. Lee, T., et al., *Transparent ITO mechanical crack-based pressure and strain sensor*. Journal of Materials Chemistry C, 2016. **4**(42): p. 9947–9953.
 79. Kim, T., et al., *Electrostatic spray deposition of highly transparent silver nanowire electrode on flexible substrate*. ACS applied materials & interfaces, 2013. **5**(3): p. 788–794.
 80. De, S., et al., *Silver nanowire networks as flexible, transparent, conducting films: extremely high DC to optical conductivity ratios*. ACS nano, 2009. **3**(7): p. 1767–1774.
 81. Lutey, A.H., *An improved model for nanosecond pulsed laser ablation of metals*. Journal of Applied Physics, 2013. **114**(8): p. 083108.
 82. Hong, S., et al., *Highly stretchable and transparent metal nanowire heater for wearable electronics applications*. Advanced materials, 2015. **27**(32): p. 4744–4751.
 83. Hsu, P.-C., et al., *Personal thermal management by metallic nanowire-coated textile*. Nano letters, 2015. **15**(1): p. 365–371.
 84. Zhu, B., et al., *Skin-inspired haptic memory arrays with an electrically reconfigurable architecture*. Advanced Materials, 2016. **28**(8): p. 1559–1566.
 85. Hattori, Y., et al., *Multifunctional skin-like electronics for quantitative, clinical monitoring of cutaneous wound healing*. Advanced healthcare materials, 2014. **3**(10): p. 1597–1607.
 86. Kim, D.-H., et al., *Epidermal electronics*. science, 2011. **333**(6044): p. 838–843.
 87. Drack, M., et al., *An imperceptible plastic electronic wrap*. Advanced Materials, 2015. **27**(1): p. 34–40.
 88. Someya, T., S. Bauer, and M. Kaltenbrunner, *Imperceptible organic electronics*. MRS Bulletin, 2017. **42**(2): p. 124–130.
 89. Someya, T., et al., *Conformable, flexible, large-area networks of pressure and thermal sensors with organic transistor active matrixes*. Proceedings of the National Academy of Sciences, 2005. **102**(35): p. 12321–12325.
 90. Nawrocki, R.A., et al., *300-nm Imperceptible, Ultraflexible, and Biocompatible e-Skin Fit with Tactile Sensors and Organic Transistors*. Advanced Electronic Materials, 2016. **2**(4): p. 1500452.
 91. Lee, W., et al., *Transparent, conformable, active multielectrode array using organic electrochemical transistors*. Proceedings of the National Academy of Sciences, 2017. **114**(40): p. 10554–10559.
 92. Choi, S., et al., *Highly conductive, stretchable and biocompatible Ag–Au core–sheath nanowire composite for wearable and implantable bioelectronics*. Nature nanotechnology, 2018. **13**(11): p. 1048–1056.
 93. Monteiro-Riviere, N.A., et al., *Protein binding modulates the cellular uptake of silver nanoparticles into human cells: implications for in vitro to in vivo extrapolations?* Toxicology letters, 2013. **220**(3): p. 286–293.

94. Hwang, D.-G., K. Trent, and M.D. Bartlett, *Kirigami-inspired structures for smart adhesion*. ACS applied materials & interfaces, 2018. **10**(7): p. 6747–6754.
95. Zhao, R., et al., *Kirigami enhances film adhesion*. Soft Matter, 2018. **14**(13): p. 2515–2525.
96. Someya, T., et al., *A large-area, flexible pressure sensor matrix with organic field-effect transistors for artificial skin applications*. Proceedings of the National Academy of Sciences, 2004. **101**(27): p. 9966–9970.
97. Jang, K.-I., et al., *Rugged and breathable forms of stretchable electronics with adherent composite substrates for transcutaneous monitoring*. Nature communications, 2014. **5**(1): p. 1–10.
98. Cheng, Y., et al., *A biomimetic conductive tendril for ultrastretchable and integratable electronics, muscles, and sensors*. ACS nano, 2018. **12**(4): p. 3898–3907.
99. Myers, A.C., H. Huang, and Y. Zhu, *Wearable silver nanowire dry electrodes for electrophysiological sensing*. Rsc Advances, 2015. **5**(15): p. 11627–11632.
100. Mishra, S., et al., *Soft, conformal bioelectronics for a wireless human-wheelchair interface*. Biosensors and Bioelectronics, 2017. **91**: p. 796–803.
101. Norton, J.J., et al., *Soft, curved electrode systems capable of integration on the auricle as a persistent brain-computer interface*. Proceedings of the National Academy of Sciences, 2015. **112**(13): p. 3920–3925.
102. Wan, D., et al., *Robust synthesis of gold cubic nanoframes through a combination of galvanic replacement, gold deposition, and silver dealloying*. Small, 2013. **9**(18): p. 3111–3117.
103. Kim, H.-J., et al., *Rubbery electronics and sensors from intrinsically stretchable elastomeric composites of semiconductors and conductors*. Science advances, 2017. **3**(9): p. e1701114.

Abstract

원 필 립
기계항공공학부 기계공학전공
서울대학교

나노 / 마이크로 스케일의 엔지니어링 구조를 통한 고 유연성 / 신축성 은 나노 와이어 기반 투명 전극 제작

차세대 전자 소자에 대한 수요가 기능성 및 고성능 장치에서 유연하고 호환되는 소자로 빠르게 변화함에 따라 신축성 전자 소자는 가볍고 유연하며 심지어 신축성이 있도록 개발되고 있다. 유연성 / 신축성 전자 소자는 최근에 기계적으로 변형 가능한 디스플레이, 웨어러블, 생체 통합 소자 및 인간과 기계를 연결하는 HMI (Human Machine Interface) 용도로서 센서를 적용하는 등 다양한 시장에 크게 확장 할 큰 잠재력을 보여주었다. 기존의 단단한 실리콘 기반 전자 장치에 비해 신축성 전자 소자는 비틀림, 구부러짐, 압축 및 스트레칭과 같은 기계적 변형에서도 기능을 유지할 수 있도록 집중하여 개발된다. 이러한 새로운 통합된 전자 시스템을 가능하게 하는 부분으로 전극을 핵심 요소로 개발하는데 이는 회로, 장치 및 센서의 필수 구성 요소로서 차지하게 된다. 이로 인해 미래의 전자 장치는 우리가 전극을 제조하고 설계하는 방법에 따라 완전히 부드럽고 상호 작용할 것이다. 따라서 유연하고 신축성있는 전극에 대한 노력은 주로 전기적 특성과 기계적 특성의 두 가지 필수 성능을 향상시키는 데 집중되어 왔다. 논문은 신축성 전자 제품의 범위를 확장하기 위해 디스플레이나 태양전지로 친숙한 투명전극을, 투명한 광학적 특성을 보여 주면서도 우수한 전기적 및 기계적 특성을 나타내는 매우 유연한 / 신축성은 나노 와이어 (AgNWs) 기반 전도성 전극 개발에 중점을 두며 서술한다.

본 논문에서는 우선적으로 은 나노와이어의 합성과정을 이해하여 다른 차원의 NW를 나노 마이크로 스케일에서 구조적 이점을 이해하여 고품질 전극을 제공하기 위해 연구한다. 그 다음 기존에 용액상태로 존재하는 나노 와이어의 이점을 활용해 대면적 공정을 시연하고, 그 공정과정에서 나노와이어

간의 접촉 저항을 극적으로 감소시키고 기판에 대한 NW의 접착력을 향상시키는 용접 / 임베딩 효과를 통해 솔루션 기반 제조 방법이 도입되었으며, 이는 기판에 팽윤성 폴리머 층을 코팅함으로써 달성된다. 이 공정을 통해 실온에서 나노 와이어 퍼콜레이션 네트워크 전극을 제조할 수 있는, 대면적 공정을 보여주었다. 마지막으로 은 나노와이어 기반 투명 유연 전극을 탄성과 신축성이 있는 전극으로 엔지니어링 하는 키리가미 설계 접근 방식이 시연되었으며, 이는 다양한 마이크로 디자인으로 설계된 이 투명 전극 패턴은 신축성 히터, 생체신호 (EP) 감지 전극 더 나아가 이를 이용한 인간-기계 인터페이스 전자 피부 (E-skin)를 포함한 일련의 웨어러블 애플리케이션에 적용될 수 있음을 보여줌으로써 유연하며 신축성까지 갖는 은 나노와이어 기반 투명전극의 다양한 가능성을 연구하였다.

주요어 : 유연 / 신축성 전극, 은 나노 와이어 (AgNW), 대면적 공정, 키리가미 디자인, 전자 스킨 (E-Skin).

학 번 : 2015-20738